Spinning of Synthetic Spider Silk-Like Fibers and *Ex Vivo* Rheology of Spider Silk

by

Nikola Kojić

B.S., Mechanical Engineering
University of California, Berkeley, 2000

Submitted to the Department of Mechanical Engineering in Partial Fulfillment of the Requirements for the Degree of Master of Science in Mechanical Engineering

at the

Massachusetts Institute of Technology

June 2003

Signature of Author .....
Department of Mechanical Engineering
March 31, 2003

Certified by .....
Gareth H. McKinley
Professor of Mechanical Engineering
Thesis Supervisor

Accepted by .....
Ain A. Sonin
Chairman, Department Committee on Graduated Students

Spinning of Synthetic Spider Silk-Like Fibers and *Ex Vivo* Rheology of Spider Silk

by

Nikola Kojic

Submitted to the Department of Mechanical Engineering
on March 31, 2003 in partial fulfillment of the
requirements for the Degree of Master of Science in
Mechanical Engineering

ABSTRACT

Spider silk has been hailed as nature's super-fiber based on its mechanical properties. A synthetic analog would have numerous applications, from the textile industry to suspension cables for bridges. This thesis discusses attempts to spin a synthetic spider silk-like material (a concentrated polyurethane solution) into fibers whose diameter is approximately that of spider silk (~1 micron). In particular, the influence of spinning conditions on fiber mechanical properties was studied. By using numerical methods to model mass transfer experiments much insight was gained on how solvent removal during elongational flow (while the fiber is on the spin line) affects mechanical properties. In order to determine solvent evaporation from the fiber during spinning, the dependence of the solvent diffusion coefficient on solvent concentration had to be obtained. This dependence was found by performing a simple experiment where a small amount of the solution was placed in a pan, which was then put in a controlled environment. The mass loss due to solvent evaporation was recorded and then modeled by using a finite element software package. A numerical algorithm was developed to determine the dependence of the solvent diffusion coefficient (through the solution) on solvent concentration that would match the

experimentally obtained mass loss curve. It was assumed that in the pan diffusion was a one-dimensional process.

Applying similar principles to a different geometry (i.e. cylindrical), and using the determined diffusion coefficient, the solvent removal from the fiber during the spinning process was modeled. Specifically, two cases were examined (a thick and thin fiber) that showed how more solvent was removed for the thinner fiber having a longer spin line. Thus, better mechanical properties were expected for the thinner fiber since more solvent was removed during elongational flow, enhancing polymer chain interactions and alignment. Mechanical tests showed that the thinner fiber had five fold better mechanical properties than the thicker fiber, indicating the importance of solvent removal.

The use of two micro-rheometric devices (a microrheometer and a capillary break-up rheometer) enabled *ex vivo* rheology measurements of a spider's spinning solution (dope). Each apparatus was designed to accommodate the small quantities (~1 microliter) available from the spider's major ampullate gland. A shear thinning behavior of the dope was observed using the microrheometer. The capillary break-up rheometer was used for extensional rheology. The rheological findings indicate potential mechanisms that could be employed by the spider to push an extremely viscous solution through a narrow spinning canal.

The results of this thesis could be used in future efforts to elucidate the spider's spinning process and to make a superior synthetic, application specific, spider silk analog.

Thesis Supervisor: Gareth H. McKinley

Title: Professor of Mechanical Engineering

Table of Contents

Acknowledgements

I would like to thank my brother Aleksandar, my mother Gordana, and my father Milos for their tremendous support over the years. I am deeply grateful to my father with whom I collaborated intensively during the past year.

I send my appreciation to my thesis advisor, Prof. Gareth McKinley, for his guidance and understanding through my graduate years at MIT. I feel very privileged to be able to work on the synthetic spider silk project, which also involved Prof. Paula Hammond, Greg Pollock, LaShanda James-Korley, and Octavia Brauner.

I am very thankful to Prof. Bora Mikic for his help with mass transfer, and Prof. David Kaplan of Tufts University for his advice regarding spider silk. I would like to thank Carlos Semino and Shuguang Zhang for their assistance with imaging of the fibers, and Sauri Gudlavalleti and Prof. Lallit Anand who helped me with the fiber mechanical tests.

I wish to acknowledge the entire McKinley group (especially José Bico) for their invaluable advice during the past 3 years. It has really been an honor to be part of the Non-Newtonian Fluids group and the Hatsopoulos Microfluids Laboratory.

Finally I would like to express gratitude to my friends from C3 for being there for me during the last six years of my life.

1 Introduction

In the past 20 years both the spider and the silkworm silk thread have received considerable attention, largely due to their mechanical properties. Spider silk has especially been at the focus of research, since its mechanical properties are unmatched by any known material. Yet, in spite of the growing interest, there remains much unknown about the process by which the spider makes the fiber. Fueling the drive to reproduce, and produce in mass quantities, the spider silk fiber is the potential for another materials revolution, much like the nylon one after WWII. Since it is not feasible to grow spiders on large farms (like silkworms) due to their cannibalistic nature and 10 fold less yield in silk than the conventional silkworm (a typical amount from one spider would be several microliters), a synthetic silk-like material is needed. In this thesis we intend to address several issues related to spinning a synthetic spider silk analog, the main being modeling of solvent removal during the spinning process. We introduce the numerical finite element method as the basis of modeling synthetic fiber spinning. In the last part of the thesis we report on rheological investigations performed on native spider silk. The *ex vivo* experiments conducted on the spinning solution provide new insight regarding the spinning process.

The thesis consists of five major parts, beginning with a chapter on background and motivation, followed by Chapter 3 dealing with numerical modeling of the diffusion coefficient for the solution used to spin synthetic fibers. Chapter 4 uses the results of Chapter 3 to model solvent removal during the synthetic spinning process and explains how solvent content relates to mechanical properties of the spun fibers. In Chapter 5 the *ex vivo* rheology of spider silk is presented. The thesis concludes with a discussion of future work in Chapter 6.

2 Background and Motivation

2.1 Spider Silk Mechanical Properties

The underlying motivation of this thesis is to produce a synthetic fiber whose mechanical properties would rival those of spider silk. This is a considerable task, since spider silk is superior to any known material [1,2]. Numerous studies have been performed on various spider types [1-5]. Although all spiders (over 30,000 known species [4]) can produce some form of silk, most of the research has focused on the orb (wheel shaped) web weaving spiders [1]. In fact, these are the most common spiders that we come in contact with daily. Their webs are specialized for catching flying insects and in turn have the most appealing mechanical properties when it comes to energy absorption [5]. One such type of spider *Araneus diadematus* (commonly known as the garden cross spider) has been studied extensively, as well as the golden orb spider *Nephila clavipes*.

There are seven different types of silk fibers produced by the araneus (Fig. 2.1). It is believed that the glands have all evolved from one type, based on the specific demands placed on the

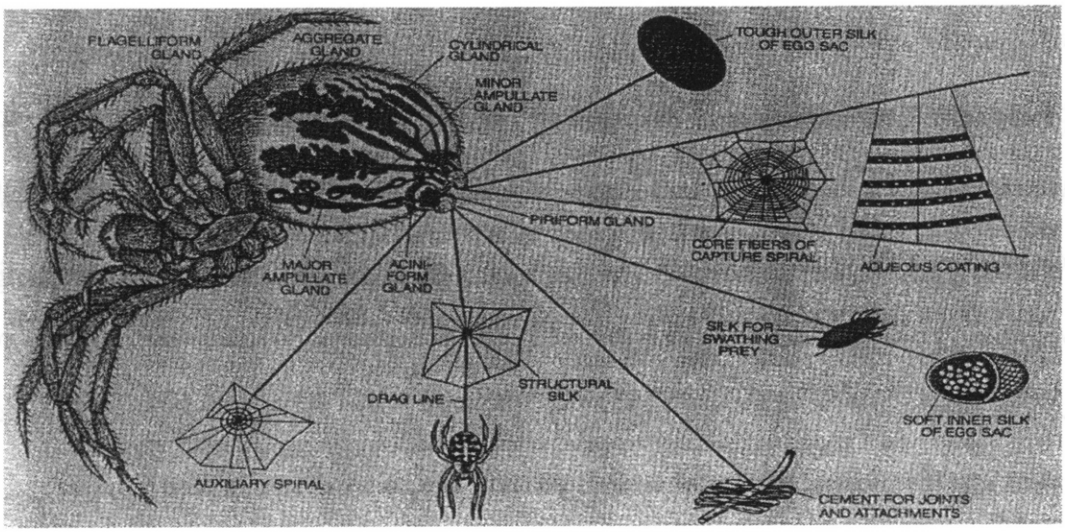

Figure 2.1 Seven types of silk from the *Araneus diadematus* [6].

spider [1]. The most studied silks have been the dragline silk (major ampullate gland) and the viscid silk (flagelliform gland) [5]. The dragline silk is used as the spider's natural 'bungee' cord and for structural support of the web, while the viscid silk is relatively more elastic and thus is used in the circular capture threads of the web. The tensile mechanical properties of these two types of threads are shown in Fig. 2.2. As the figure indicates, they have entirely different stress-strain curves, each of which is perfectly suited for the function necessitated by the successful capture of prey.

The area under the stress-strain curve represents energy per unit volume of material that the fiber can absorb before breaking, also known as toughness (T). The slope of the initial, linear part of the stress-strain curve is defined as Young's modulus of elasticity (E) and is a measure of how stiff the material is. Thus, Fig. 2.2 indicates dragline silk is much more stiff with a higher breaking stress (also known as strength) than the more extensible viscid silk.

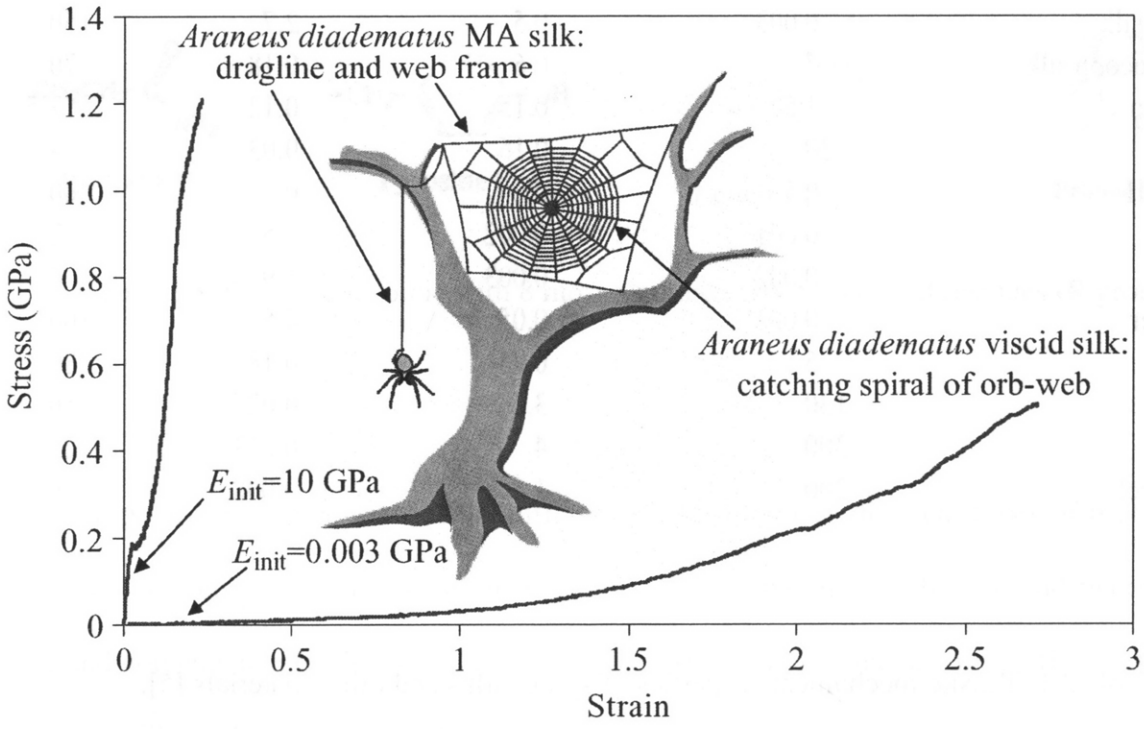

Figure 2.2 Stress-strain curves for dragline and viscid silk of *A. diadematus* [5].

Extensibility is defined as the maximum strain (change in length divided by initial fiber length) the fiber can experience before breaking. The truly superior mechanical properties of spider silk are best appreciated when compared to other materials, such as the commercial gold standard: Kevlar (Table 2.1). As the table indicates, both viscid and dragline silk combine strength and extensibility in such a way that yields unmatched toughness when compared to any known material.

Material	Stiffness, E_{init} (GPa)	Strength, σ_{max} (GPa)	Extensibility, ε_{max}	Toughness ($MJ\,m^{-3}$)
Araneus MA silk	10	1.1	0.27	160
Araneus viscid silk	0.003	0.5	2.7	150
Bombyx mori cocoon silk	7	0.6	0.18	70
Tendon collagen	1.5	0.15	0.12	7.5
Bone	20	0.16	0.03	4
Wool, 100% RH	0.5	0.2	0.5	60
Elastin	0.001	0.002	1.5	2
Resilin	0.002	0.003	1.9	4
Synthetic rubber	0.001	0.05	8.5	100
Nylon fibre	5	0.95	0.18	80
Kevlar 49 fibre	130	3.6	0.027	50
Carbon fibre	300	4	0.013	25
High-tensile steel	200	1.5	0.008	6

Table 2.1 Tensile mechanical properties of spider silks and other materials [5].

2.2 Composition and Structure of Spider Silk

Spider silk is a protein-based material. Proteins are made from a combination of amino acids and there are 20 different amino acids. Each protein has a backbone, onto which are attached amino acid residues (Fig. 2.3) [7].

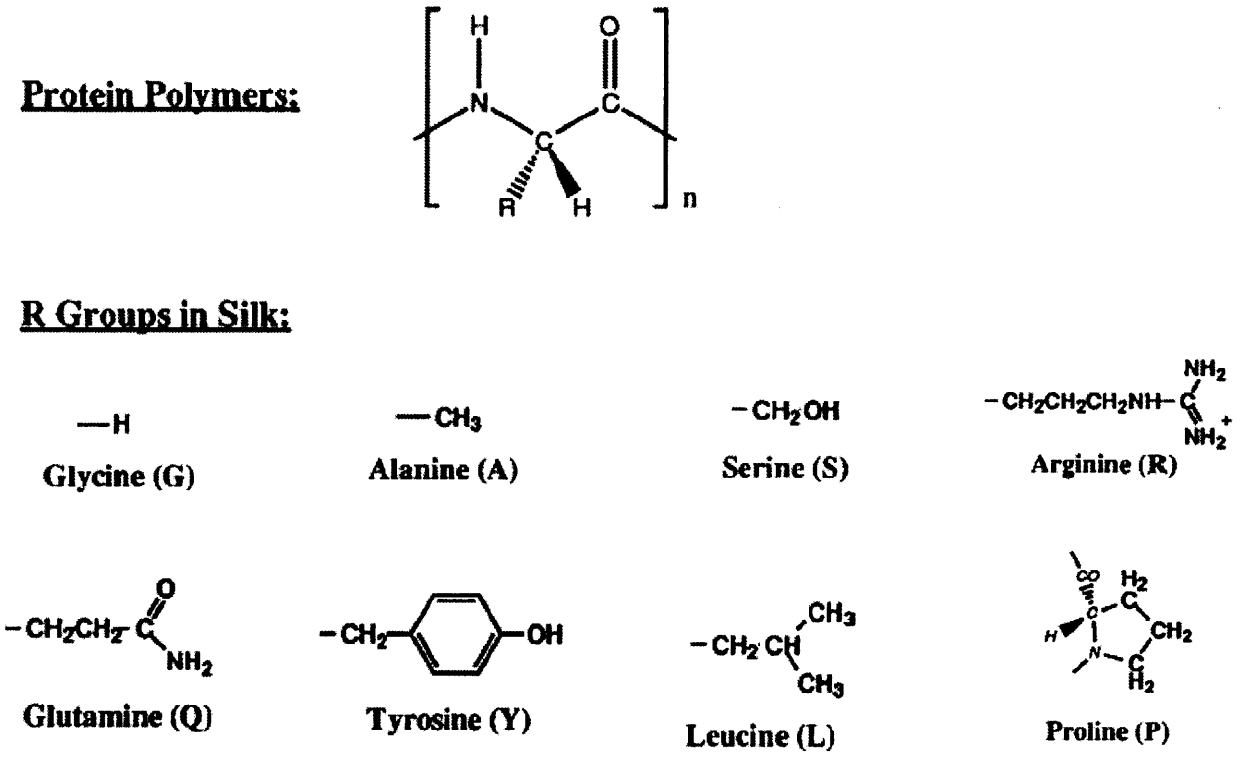

Figure 2.3 Protein backbone with 8 most abundant silk amino acid residues (R groups).

In a given spider type each of the different glands produces different types of proteins. Their amino acid composition is given in Fig. 2.4. By comparing flagelliform and major ampullate gland contents one begins to see how their corresponding mechanical properties of dragline and viscid silk can be so different (Fig. 2.2).

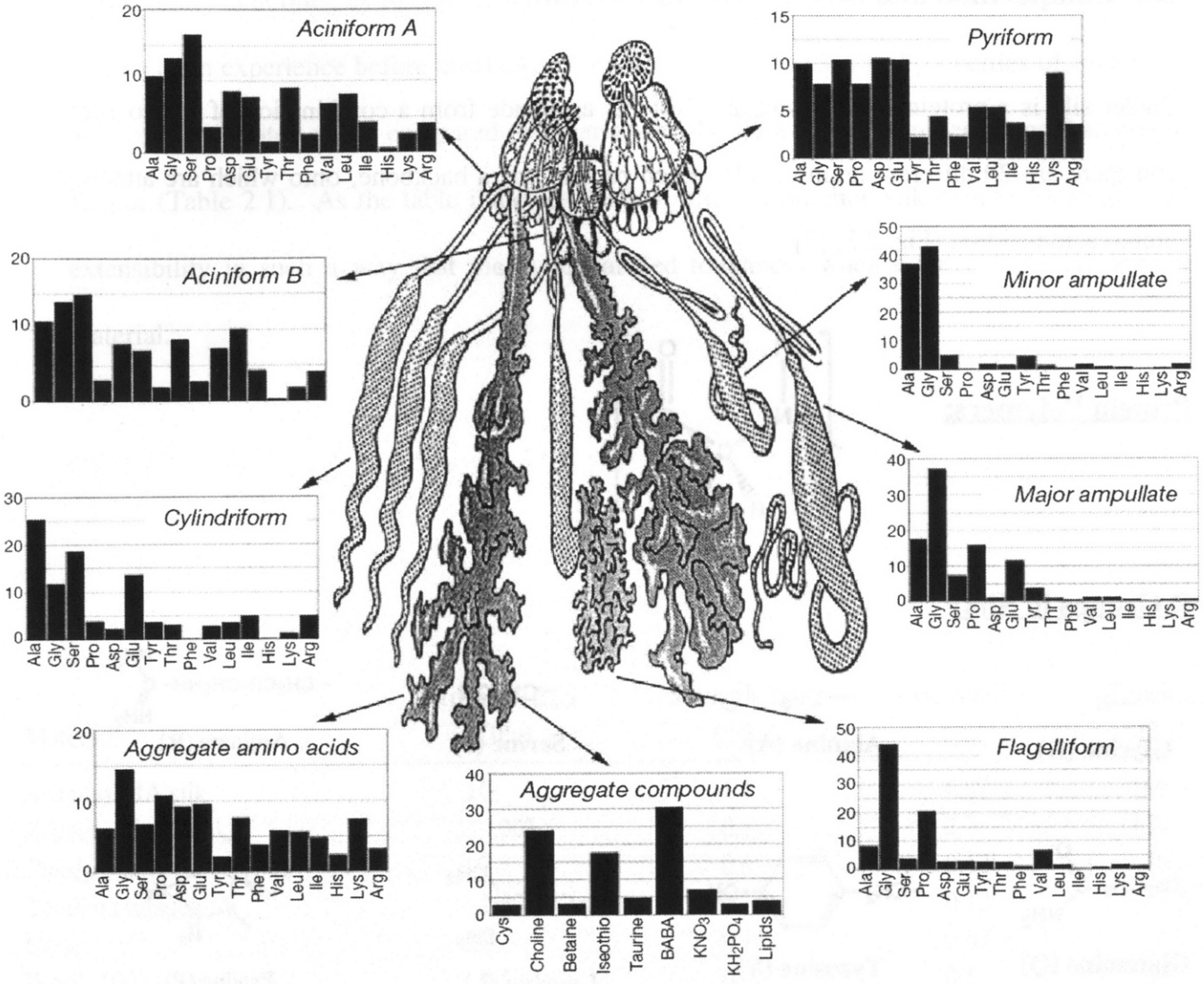

Figure 2.4 Amino acid compositions of different spider gland types [1].

The silk genes have been sequenced in an effort to better understand how the corresponding proteins could be arranged. Dragline silk is mostly composed of two proteins: Spidroin I and Spidroin II. Both of these proteins can be described as block copolymers with poly-alanine blocks (hard domains) and glycine rich, soft domains (Fig 2.5). The poly-alanine blocks consist of approximately 8 monomers, while the glycine rich domains have the glycine-glycine-X motif as the most common.

Spidroin I

Spidroin II

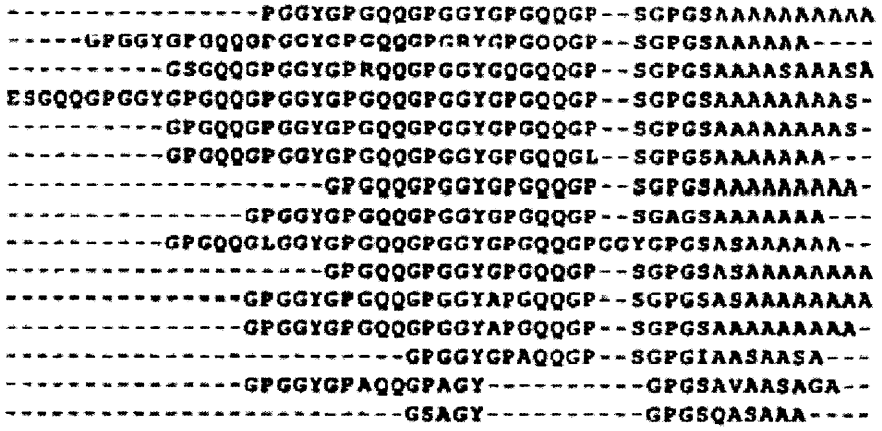

Figure 2.5 Amino acid sequence for dragline silk proteins Spidroin I and II [8].

There has been much speculation about the microstructure of the silk fiber, i.e. how the proteins fold and interact (Fig. 2.6). The exact microstructure remains unknown and a constant source of research [9,10]. The silk genes have been cloned and expressed in yeast, but the resulting proteins had no structural resemblance to the spun fiber, forming only a glassy and brittle material [11]. Thus, the spinning process plays the key role in folding the silk proteins into their appropriate conformations. Therefore, if one is to reproduce spider silk by a synthetic material the spinning process must be elucidated.

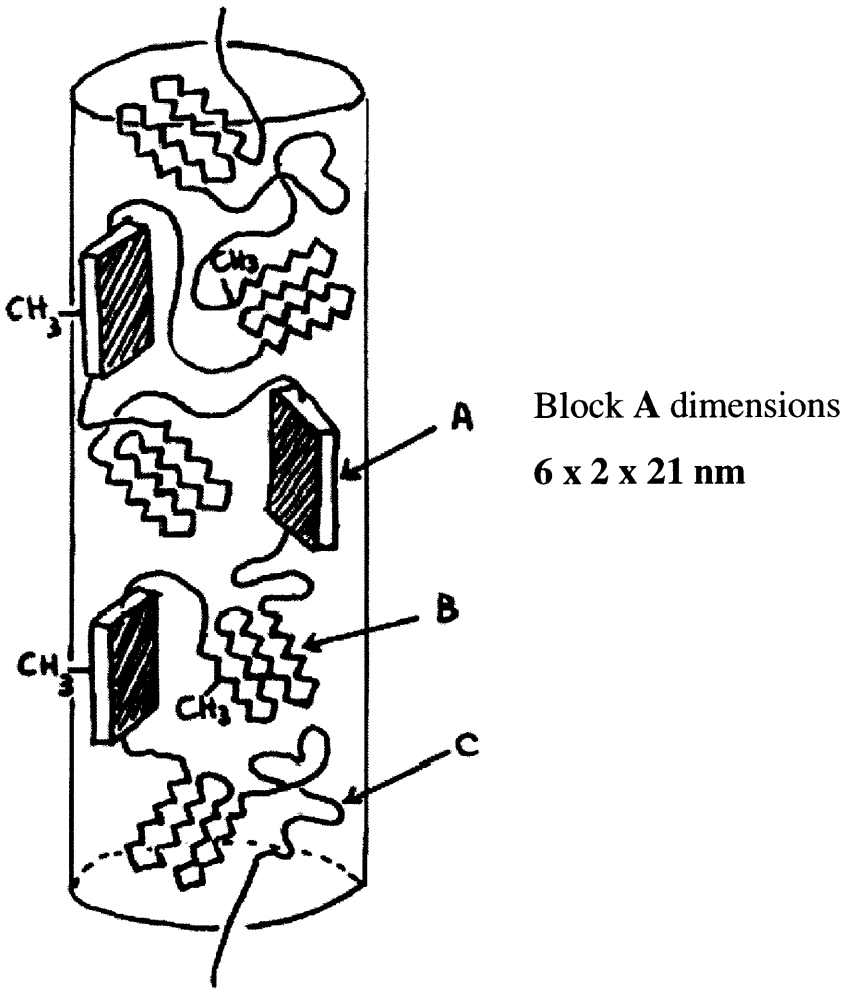

Figure 2.6 A proposed microstructure of spider silk. A: highly ordered poly-alanine hard domains, B: weakly oriented sheets, C: glycine-rich matrix [8].

2.3 A Potential Application: Stopping a Boeing 747

The spider silk thread combines strength and extensibility so as to maximize the area under its stress-strain curve and thus maximizes the energy absorbed before breaking (Fig. 2.2, Table 2.1). Thus, commercially available silk could be used in many applications, ranging from lightweight bulletproof vests, to artificial human ligaments, to suspension cables for bridges. Essentially any application requiring a lightweight material optimized for energy absorption would be ideally suited for spider silk.

One example often used to convey the remarkable mechanical properties of spider silk to the general public has been the idea that a pencil thick spider silk fiber could be used to stop a Boeing 747 plane in mid-flight. An analysis of this statement, including how much of the thread is needed follows.

The natural spider silk thread diameter is on the order of 1 micron and a typical diameter of a fly flying into (and being caught by) the web is about 1cm:

$$\frac{d_{web}}{D_{fly}} \sim \frac{10^{-4} cm}{1 cm} = 10^{-4} \tag{2.1}$$

Thus, based on this over-simplistic scaling argument, a 1cm diameter thread would correspond to a fly of 100m being caught in the web.

$$\frac{d_{web}}{D_{fly}} = 10^{-4} \Rightarrow D_{fly} = \frac{d_{web}}{10^{-4}} = \frac{1 cm}{10^{-4}} = 10^{4} cm = 100 m \tag{2.2}$$

Therefore, it seems the statement could be true, since a Boeing 747 has a wingspan of about 65 meters.

For a more rigorous proof, the mechanical properties of the silk thread are employed along with the data for a flying Boeing 747. For dragline silk, the measured toughness is 160 MJ/m^3 (which

is close to the 150 MJ/m^3 toughness of viscid silk from Table 2.1) and we assume a Boeing 747 weighing 400 tons flies at a cruising speed of 253 m/s. Then, to stop the plane all of the plane's kinetic energy must be absorbed by the fiber

$$E_{kinetic} = E_{silk}$$
$$\frac{mv^2}{2} = TV \tag{2.3}$$

where m is the mass of the plane, v is the plane velocity, T is the toughness of spider silk, and V is the volume of the fiber. After substitution of the above values, the required volume is found

$$V = (1/2)\ 4\times10^5(253)^2/(160\times10^6) \approx\ 80\,m^3 \tag{2.4}$$

Since the length L of a 1cm diameter (pencil diameter) fiber is needed, it follows that

$$V = (1/4)\ \pi\ d^2_{pencil}\ L$$
$$L = (4\times80)/(\pi\times10^{-4}) \approx 10^6\ m \tag{2.5}$$

Therefore, the required pencil-diameter thread must be 10^6 meters long, or about 600 miles! Packaging a total of 10^6 meters into a web of radial and circumferential threads would mean that

$$L_{total} = L_{rad} + L_{circ} = 10^6\,m \tag{2.6}$$

Focusing first on the radial spokes the number of radial strands for a given spacing of Δs (see Fig 2.7) along the circumference is

$$n_{radial} = \frac{\pi\ D_{web}}{\Delta s} \tag{2.7}$$

Thus, since each individual radial spoke has a length equal to the web diameter, the total length needed for the radial spokes is

$$L_{rad} = n_{rad} D_{web} = \frac{\pi D_{web}^2}{\Delta s} \tag{2.8}$$

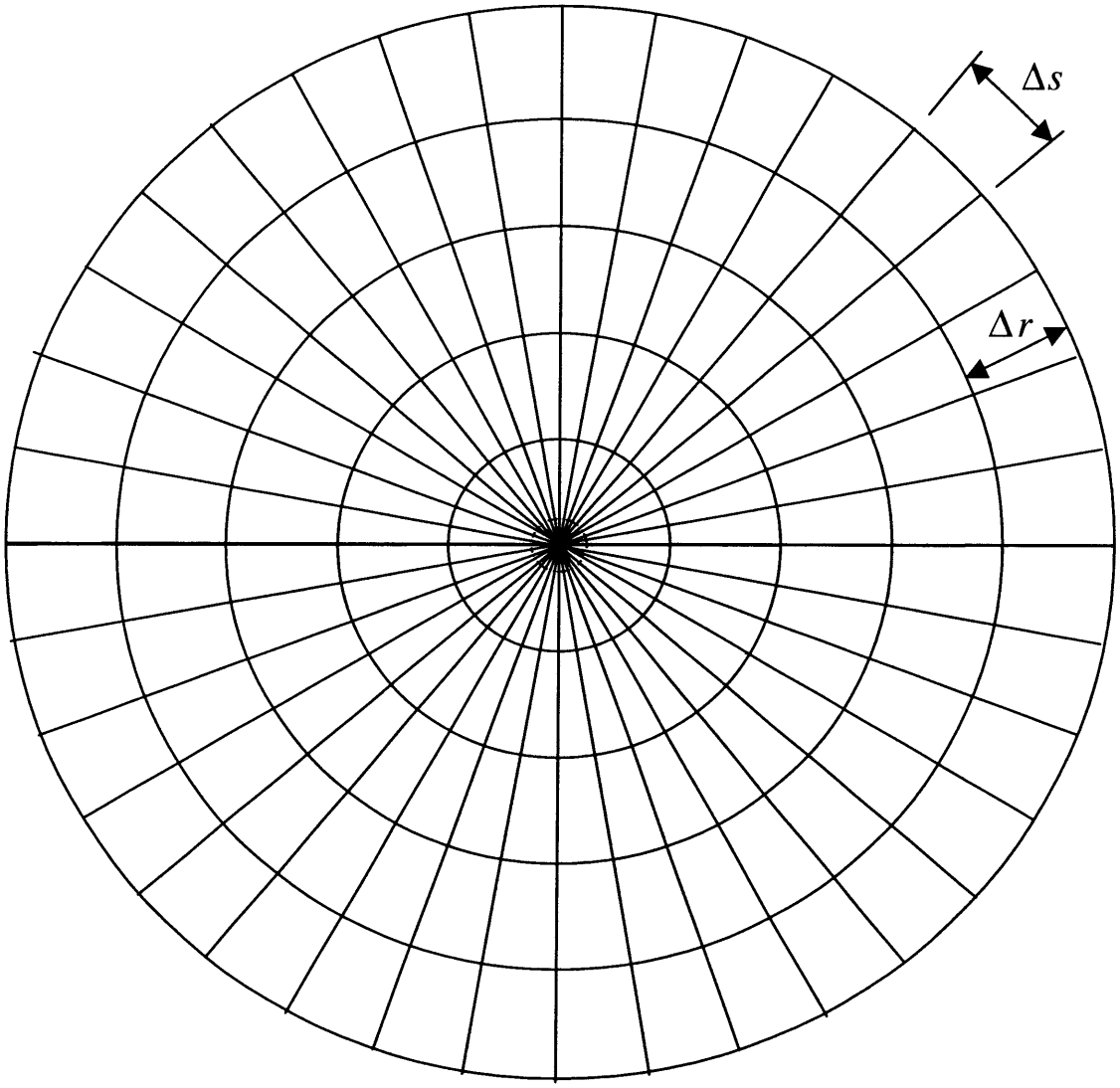

Figure 2.7 A spider web design for catching a Boeing 747.

The circumferential threads are concentric circles spaced a distance of Δr from each other (see Fig. 2.7). Then the number of concentric circles is

$$n_{circ} = \frac{D_{web}/2}{\Delta r} \tag{2.9}$$

Summing the lengths of all of the circumferential threads gives

$$L_{circ} = \pi\left[D_{web} + (D_{web} - 2\Delta r) + (D_{web} - 4\Delta r) + \ldots + 2\Delta r\right] \tag{2.10}$$

This expression can then be written in more compact form

$$L_{circ} = \pi \sum_{k=0}^{n_{circ}-1} \left(D_{web} - 2k\Delta r\right) \tag{2.11}$$

Thus the final expression for the total length based on equations (2.8), (2.9), (2.11)

$$L_{total} = L_{rad} + L_{circ} = \frac{\pi D_{web}^2}{\Delta s} + \sum_{k=0}^{D_{web}/2\Delta r-1} \pi\left(D_{web} - 2k\Delta r\right) \tag{2.12}$$

Now going back to the plane problem, a Boeing 747 has a wingspan of about 65m and in order to catch it in a web the diameter of the web must be greater than 65m.

Based on equation (2.12) we give the following two web designs

1) $D_{web} = 100m$, $\Delta r = \Delta s = 4\ cm \quad \Rightarrow \quad L_{tot} = 9.82\times10^5\ m$

2) $D_{web} = 200m$, $\Delta r = \Delta s = 15\ cm \quad \Rightarrow \quad L_{tot} = 1.05\times10^6\ m$

Thus, both of the webs would approximately use all of the necessary thread length of 10^6 meters to catch the Boeing 747 in mid-flight.

It is obvious that obtaining $80m^3$ of silk necessary for this web construction, Eq. (2.4), would be a daunting task requiring harvesting silk daily from one million spiders that each produce 1 microliter per day for about 220 years – hence the evident need for a synthetic spider silk analog.

References:

[1] Vollrath F., Knight D.P. Liquid crystalline spinning of spider silk. *Nature* **410**, p541-548 (2001).

[2] Shao Z., Vollrath F. Surprising strength of silkworm silk. *Nature* **418**, p741 (2002).

[3] Kaplan D., Adams W.W., Farmer B., Viney C. *Silk Polymers. Materials Science and Biotechnology* (American Chemical Society, Washington, 1994).

[4] Kaplan D., Mello C.M.., Aciadiacono S., Fossey S., Senecal K., Muller W. *Silk. Protein-Based Materials*. McGrath K. and Kaplan D. (Birkhauser, Boston, 1997).

[5] Gosline J.M., Guerrete P.A., Ortlepp C.S., Savage K.N. The mechanical design of spider silks: from fibroin sequence to mechanical function. *The Journal of Experimental Biology* **202**, 3295-3303 (1999).

[6] Vollrath F. Spider Webs and Silks. *Scientific American* , p70-76 (March 1992).

[7] O'Brien J.P., Fahnestock S.R., Termonia Y., Gardner K.H. Nylons from Nature: Synthetic Analogs to Spider Silk. *Advanced Materials* **10**, p1185-1195 (1998).

[8] Heslot H. Artificial fibrous proteins: A review. *Biochimie* **80**, p19-31 (1998).

[9] van Beek J.D., Hess S., Vollrath F., Meier B.H. The molecular structure of spider dragline silk: Folding and orientation of the protein backbone. *PNAS* **99**, p10266-10271 (2002).

[10] Hayashi C.Y., Shipley N.H., Lewis R.V. Hypothesis that correlate the sequence, structure, and mechanical properties of spider silk proteins. *International Journal of Biological Macromolecules* **24**, p271-275 (1999).

[11] Lazaris A., Arcidiacono S., Huang Y., Zhou J., Duguay F., Chretien N., Welsh E., Soares J., Karatzas C. Spider Silk Fibers Spun from Soluble Recombinant Silk Produced in Mammalian Cells. *Science* **295**, p472-476 (2002).

3 Numerical Determination of the Solvent Diffusion Coefficient for a Concentrated Polymer Solution

Abstract

Diffusion of solvent through a concentrated polymer solution can be modeled by Fick's law. The material parameter in this law is the solvent diffusion coefficient, which can be a function of solvent concentration. We propose a numerical procedure to obtain the dependence of the diffusion coefficient upon solvent concentration. The procedure employs the finite element method to model a simple pan weighing experiment. In this experiment a small amount of the polymer solution is placed in a pan and allowed to evaporate into air, while recording the mass loss over time. Using the proposed procedure the diffusion coefficient as a function of solvent concentration is obtained, such that the computed mass loss matches the experimental results.

3.1 Introduction

In many chemical engineering applications, such as dry spinning of fibers out of a concentrated polymer solution with evaporation of solvent, diffusion is the governing process. The internal diffusion of solvent molecules through the polymer solution is modeled by Fick's law, in which the diffusion coefficient is the material parameter [2,5,10,11]. When polymer solutions experience significant changes in solvent concentration due to mass transfer, the diffusion coefficient can vary considerably as a function of solvent concentration [6,11]. Therefore, the essential problem becomes establishing the dependence of the diffusion coefficient upon solvent concentration.

In this paper we describe how to obtain such a dependence by finite element modeling of a simple evaporation experiment. A small amount of the solution was placed in a pan and allowed to evaporate into air, while measuring mass loss over time. The governing process occurring within the polymer solution is diffusion, while convection dominates on the vapor (air) side. We model this process by imposing the appropriate boundary conditions and present a computational procedure to numerically determine the diffusion coefficient of solvent through the polymer solution as a function of solvent concentration. Subsequently, the dependence of the diffusion coefficient upon concentration enables the calculation of the time evolution of solvent concentration profiles along the depth of the pan.

The chapter is organized as follows. The next section briefly describes the basic pan-experiment, followed by a discussion of the governing process in Section 3.3. The computational procedure is presented in Section 3.4, and numerical results are given in Section 3.5. Finally, we conclude by touching on practical applications of the proposed computational procedure.

3.2 Experimental Procedure

The polymer solution described in this chapter consists of 35 % polymer and 65% solvent by weight (Table 3.1). We will further refer to the THF/DMAc system as solvent, and the Elasthane/PTMO system as polymer. The solution was placed in a Seiko TG/DTA–320 (Thermogravimetric and Differential Thermal Analyzer) machine, which was used to record mass as a function of time for 12200 seconds (3.4 hrs). A 5 mm diameter aluminum pan was used to hold an initial amount of 19.912mg of the solution. The TG/DTA provided a closed environment at a temperature of T = 25°C, while blowing air at a rate of 150 mL/min. Mass loss was recorded on the computer using the standard Seiko TG/DTA software (Fig. 3.1).

Table 3.1 Composition of Polymer Solution

35 % Polymer *	**65 % Solvent**
20 % Elasthane 80A**	90 % THF
15 % PTMO-2900	10 % DMAc

*All percentages in weight percent.

** **Elasthane™** 80A polyurethane is a thermoplastic elastomer formed as the reaction product of a polyol, an aromatic diisocyanate, and a low molecular weight glycol used as a chain extender. Polytetramethylene oxide (PTMO) is reacted in the bulk with aromatic isocyanate, 4,4'-methylene bisphenyl diisocyanate (MDI), and chain extended with 1,4-butanediol. The Polymer Technology Group, Berkeley, California. http://www.polymertech.com/

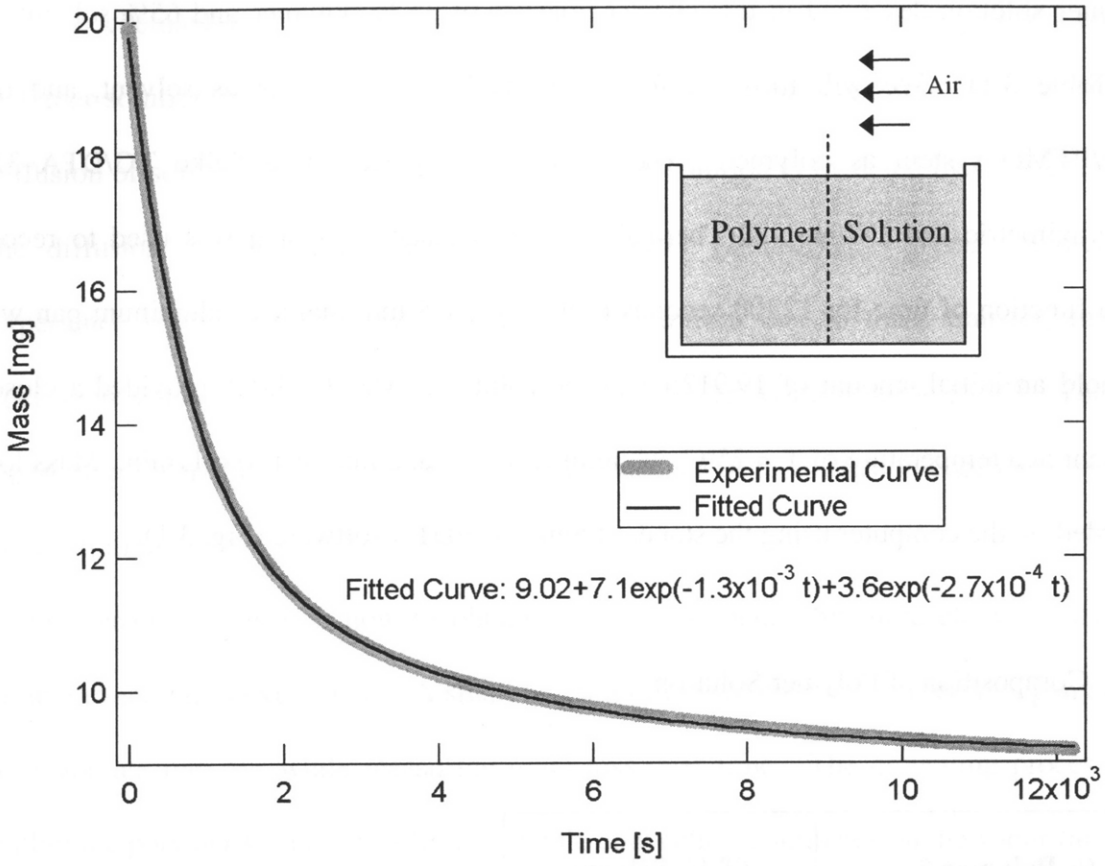

Figure 3.1 Mass change over time of the polymer solution used in the pan experiment.

3.3 Determining the Governing Process

In order to leave the polymer solution, the solvent molecules must first migrate to the surface and then evaporate into the air. The migration to the surface corresponds to what is called internal diffusion, while the evaporation from the surface is related to convective mass transfer. For a rapid convective removal, as is the case in our experiment, we have a much greater resistance encountered on the internal (solution) side than on the convective (vapor/air) side. The ratio of the resistances is commonly referred to as the mass transfer Biot number [10]:

$$Bi_m = \frac{h_m \alpha L}{D_{ss}} \tag{3.1}$$

where D_{SS} is the internal solvent diffusion coefficient $\left[mm^2/s\right]$, h_m is the convective mass transfer coefficient $\left[mm/s\right]$, L is the characteristic length $[mm]$, and α is the partition coefficient between the two phases at the interface. For our case, an order of magnitude estimate gives:

$$D_{ss} \sim 10^{-5} \frac{mm^2}{s} \quad , \quad h_m \sim 1 \frac{mm}{s}$$
$$L \sim 1\, mm \quad , \quad \alpha \sim 10^{-3} \tag{3.2}$$

The corresponding Biot number then becomes $Bi_m \sim 100$. This high value of the Biot number implies that the governing process is internal diffusion [10,11].

3.4 Computational Procedure

In this section we first give the fundamental diffusion equation for the pan experiment conditions, then summarize the relevant finite element equations, and present the computational procedure. The diffusion of a solvent through a polymer solution is governed by the general form of Fick's law [11]

$$\frac{\partial \rho_s}{\partial t} = \nabla[\rho_T D_{ss} \nabla(\frac{\rho_s}{\rho_T})] \tag{3.3}$$

where ρ_s is the partial mass density (further referred to as concentration) of the solvent, ρ_T is the total mass density (mass per unit volume of solution),

$$\rho_T = \rho_s + \rho_p \tag{3.4}$$

with ρ_p being the concentration (partial mass density) of the polymer. As stated above, it is assumed that

$$D_{ss} = D_{ss}(\rho_s) \tag{3.5}$$

The diffusion of solvent in the pan experiment can be considered a 1-D process, for which the model is shown in Fig. 3.2.

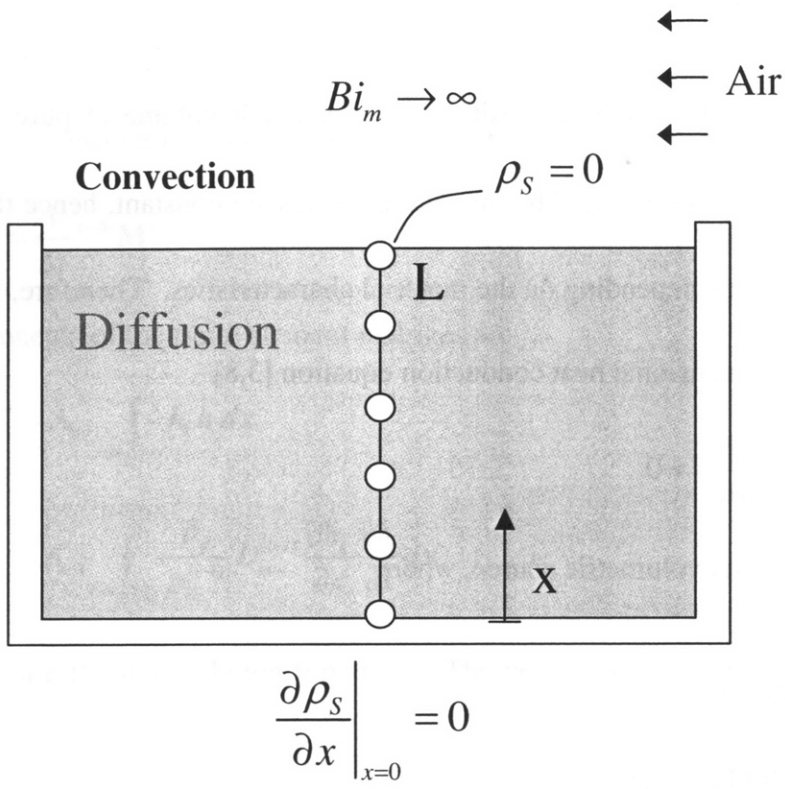

Figure 3.2 Finite element model of the pan experiment

The spatial derivatives in Eq. (3.3) then reduce to the partial derivatives with respect to the x-coordinate, hence

$$\frac{\partial \rho_s}{\partial t} - \frac{\partial}{\partial x}\left[\rho_T D_{SS} \frac{\partial}{\partial x}\left(\frac{\rho_s}{\rho_T}\right)\right] = 0 \qquad (3.6)$$

In order to transform the expression in brackets we use the following relation

$$\rho_T = (1-\frac{\overline{\rho}_p}{\overline{\rho}_s})\rho_s + \overline{\rho}_p = a_1\rho_s + a_2 \tag{3.7}$$

where $\overline{\rho}_s$ and $\overline{\rho}_p$ are the material densities (mass per unit volume of pure substance) of the solvent and polymer, respectively. The material densities are constant, hence the coefficients a_1 and a_2 are two constants depending on the material characteristics. Therefore, Eq. (3.6) takes on the form of the one-dimensional heat conduction equation [3,8]

$$\frac{\partial \rho_s}{\partial t} - \frac{\partial}{\partial x}(\alpha_m \frac{\partial \rho_s}{\partial x}) = 0 \tag{3.8}$$

with no heat (here mass) volumetric source, where

$$\alpha_m = a_2 \frac{D_{ss}}{a_1\rho_s + a_2} \tag{3.9}$$

is the variable depending on ρ_s.

The usual Galerkin procedure [3,4,8] is employed to transform Eq. (3.8) into the finite element balance equations. Thus, the integration over finite element volume V of Eq. (3.8) gives

$$\int_V \frac{\partial \rho_s}{\partial t} dV - \int_V \frac{\partial}{\partial x}(\alpha_m \frac{\partial \rho_s}{\partial x}) dV = 0 \tag{3.10}$$

where $dV = Adx$, with A being the element cross-section area. By linearization around the time "t" a system of algebraic incremental equations is obtained. An incremental-iterative form of these equations, assuming an implicit integration scheme (i.e. the equilibrium is sought iteratively for the end of time step), can be written as [1,8,9]

$${}^{t+\Delta t}\hat{\mathbf{K}}^{(i-1)} \Delta \boldsymbol{\rho}_s^{(i)} = {}^{t+\Delta t}\mathbf{F}^{(i-1)} - {}^{t+\Delta t}\hat{\mathbf{K}}^{(i-1)} \, {}^{t+\Delta t}\boldsymbol{\rho}_s^{(i-1)} \tag{3.11}$$

where "i" denotes the iteration counter, and the index "$t+\Delta t$" indicates that the evaluation is performed at the end of time step. The vectors ${}^{t+\Delta t}\boldsymbol{\rho}_s^{(i-1)}$ and $\Delta\boldsymbol{\rho}_s^{(i)}$ are the nodal vectors for the concentrations and concentration increments. The matrix ${}^{t+\Delta t}\hat{\mathbf{K}}^{(i-1)}$ is

$$ {}^{t+\Delta t}\hat{\mathbf{K}}^{(i-1)} = \frac{1}{\Delta t}\,{}^{t+\Delta t}\mathbf{M}^{(i-1)} + {}^{t+\Delta t}\mathbf{K}^{(i-1)} \tag{3.12} $$

where the components of the finite element matrices are

$$ {}^{t+\Delta t}M_{kl}^{e(i-1)} = A_{i-1}\int_{{}^{t+\Delta t}L^{(i-1)}} h_k h_l\, dx \tag{3.13} $$

$$ {}^{t+\Delta t}K_{kl}^{e(i-1)} = A_{i-1}\int_{{}^{t+\Delta t}L^{(i-1)}} \frac{\bar{\rho}_p}{\rho_T^{(i-1)}} D_{ss}^{(i-1)} \frac{\partial h_k}{\partial x}\frac{\partial h_l}{\partial x} dx \tag{3.14} $$

Here, h_k and h_l are the interpolation functions. The vector ${}^{t+\Delta t}\mathbf{F}^{(i-1)}$ is the mass flux through the boundary, i.e.

$$ F_k^{(i-1)} = \int_{A_{i-1}} h_k\, q_A\, dA \tag{3.15} $$

where q_A is the mass flux through current area A_{i-1}. In our case the element area A is constant, while the element lengths change. Hence, the line integrals are evaluated over the last known element length, calculated as

$$ {}^{t+\Delta t}L^{(i-1)} = L_p + \frac{1}{\bar{\rho}_s}\int_{{}^{t+\Delta t}L^{(i-2)}} {}^{t+\Delta t}\rho_s^{(i-1)} dx \tag{3.16} $$

where $L_p = \left({}^0\rho_p/\bar{\rho}_p\right){}^0L$ is the length of the finite element occupied by the polymer, which does not change. The iterations in Eq. (3.11) continue until a selected numerical tolerance is reached, e.g. $\left\|\Delta\boldsymbol{\rho}_s^{(i)}\right\| \le \varepsilon$, where ε is a small number.

Using the above finite element equations the dependence of $D_{ss}(\rho_s)$ can be obtained. We propose the following two procedures:

a) calculation of the dependence $(D_{ss})_{mean}$ on the $(\rho_s)_{mean}$

b) determination of $D_{ss}(\rho_s)$ that matches the experimental results.

Computational steps used in procedure a) are given in Fig. 3.3.

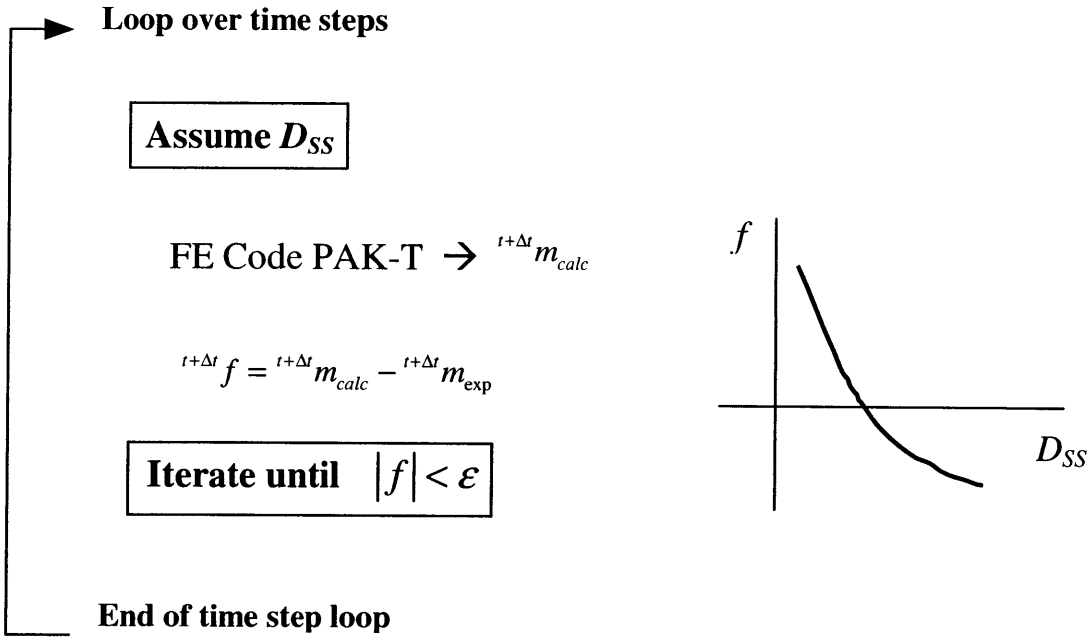

Figure 3.3 Computational steps to determine dependence $(D_{ss})_{mean}$ on $(\rho_s)_{mean}$

As shown in the Fig 3.3, a value of D_{ss}, denoted here as $(D_{ss})_{mean}$, is assumed for the current time step and this value is the same for all material points. We then iterate on $(D_{ss})_{mean}$ until the total mass of the polymer solution ${}^{t+\Delta t}m_{calc}$ matches the experimental value ${}^{t+\Delta t}m_{\exp}$ at the end of the time step. The corresponding mean solvent concentration $(\rho_s)_{mean}$ is defined as

$$(\rho_s)_{mean} = \frac{\sum_{elements} \int_{L_{element}} \rho_s \, dx}{\sum_{elements} L_{element}} \tag{3.17}$$

The iterations continue until the equation

$${}^{t+\Delta t}f = {}^{t+\Delta t}m_{calc} - {}^{t+\Delta t}m_{\exp} = 0 \tag{3.18}$$

is satisfied, where

$${}^{t+\Delta t}m_{calc} = A \sum_{elements} \int_{{}^{t+\Delta t}L} {}^{t+\Delta t}\rho_s dx + m_p \tag{3.19}$$

Here, A is the cross-sectional area of the pan, and m_p is the total mass of polymer. The iterations according to Eq. (3.11) are performed for each trial value of $(D_{ss})_{mean}$.

In the computational procedure b) an initial assumption of $D_{ss}(\rho_s)$ is made, and then modified to satisfy the experimentally recorded $m_{\exp}(t)$. We start with the dependence $(D_{ss})_{mean}$ on $(\rho_s)_{mean}$, which is first approximated as linear, then changed to bilinear, and ultimately to a multilinear relationship in order to satisfy the equation $m_{calc} = m_{\exp}$ in the whole time domain. The modifications of the $D_{ss}(\rho_s)$ dependence were based on a trial-and-error process.

3.5 Numerical Results

The following example is shown as an illustration of the proposed computational scheme. The basic FE code PAK-T [7] for heat conduction, with necessary modifications, is employed. A simple bisection method with an acceleration scheme is used to determine the trial values of $(D_{ss})_{mean}$ for solving Eq. (3.18). The materials used in the experiment are described in Section 3.2. The data are as follows (densities in $[\, g / cm^3 \,]$ and length in $[cm]$)

$$\bar{\rho}_s = 0.894 \qquad \bar{\rho}_p = 1$$

$$^0\rho_s = 0.603 \qquad ^0\rho_p = 0.325$$

$$^0L = 0.112$$

The experimental mass loss $m_{\exp}(t)$ is shown in Fig. 3.1. The finite element model, along with the appropriate boundary conditions, is depicted in Fig. 3.2. The boundary conditions are:

1) $(\rho_S)_{surface} = 0$

2) $\left.\dfrac{\partial \rho_S}{\partial x}\right|_{x=0} = 0$

The first boundary condition follows from the high value of the Biot number, while the second boundary condition comes from the impermeability of the pan.

Figure 3.4 displays the dependence $(D_{ss})_{mean}$ on $(\rho_s)_{mean}$ as the result of the computational procedure a). The dependence seems almost linear for a wide range of solvent concentrations. This linear relationship is then used as a starting point for the trial-and-error process in procedure b).

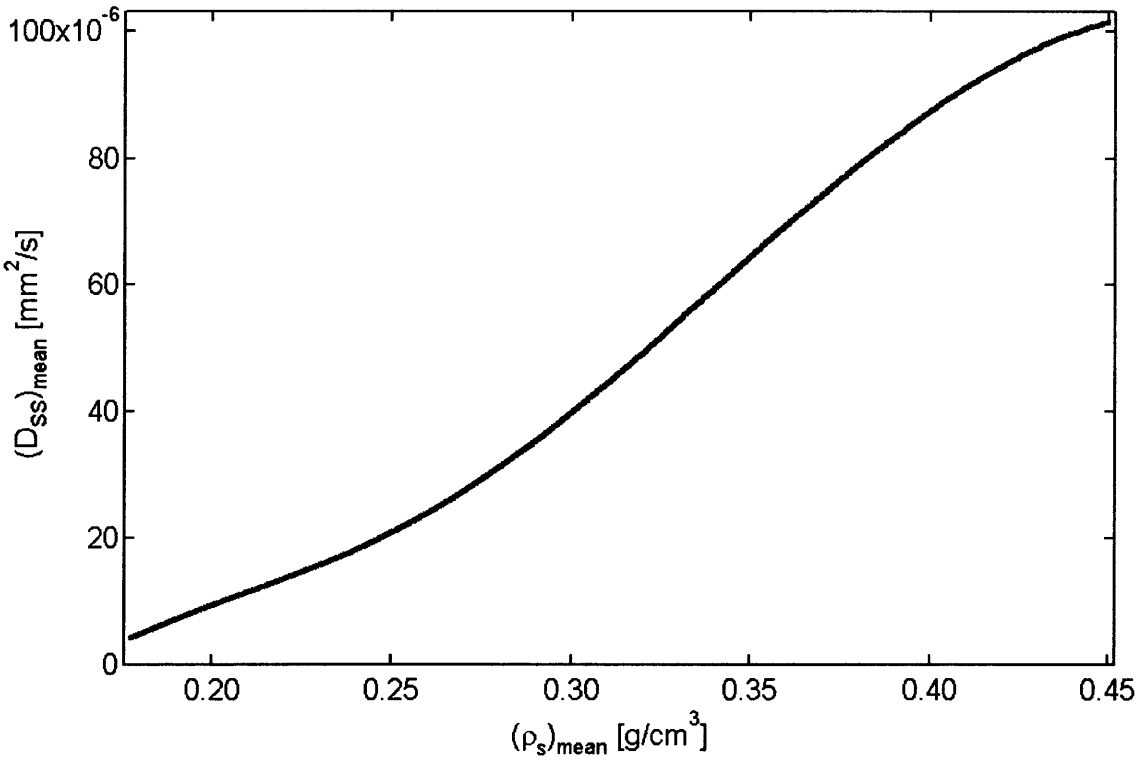

Figure 3.4 Dependence of $(D_{ss})_{mean}$ on $(\rho_s)_{mean}$ according to procedure a).

Figure 3.5 shows the dependence of the solvent diffusion coefficient D_{ss} on the solvent concentration ρ_s obtained by trial-end-error based on procedure b).

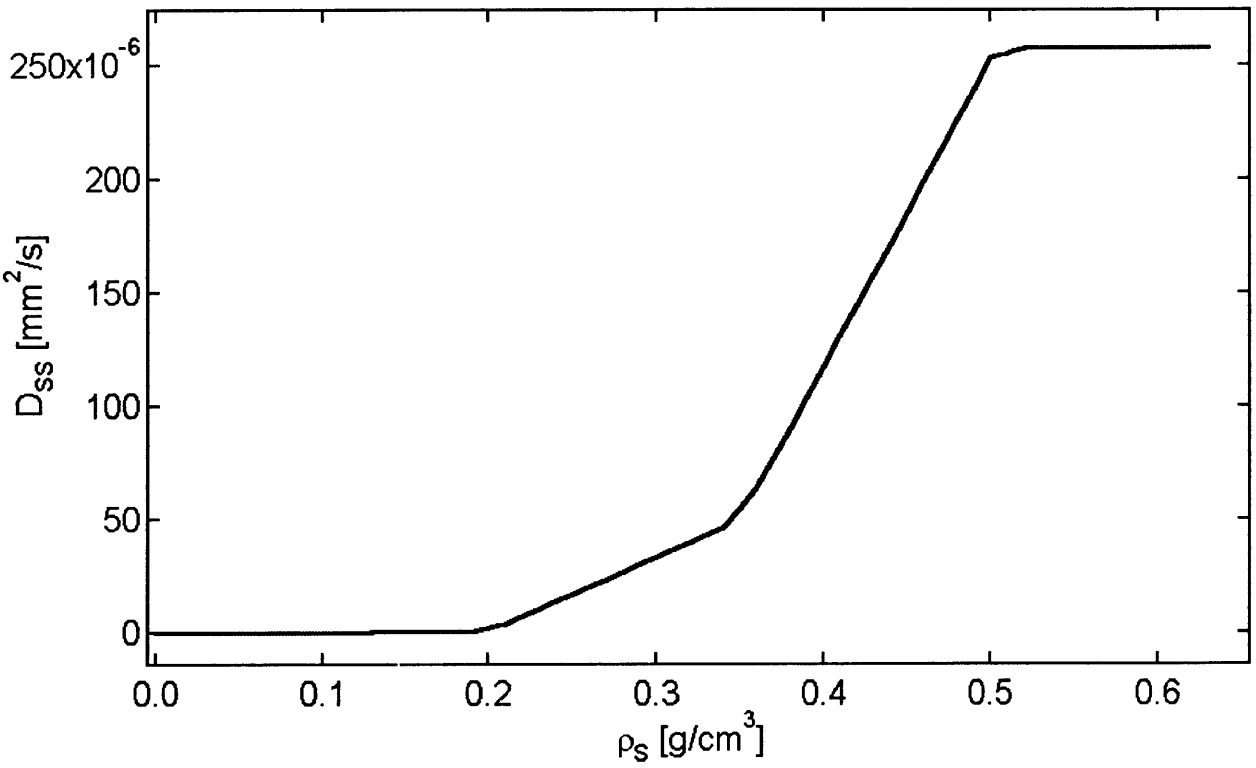

Figure 3.5 Solvent diffusion coefficient D_{ss} vs. solvent concentration ρ_s obtained by trial-and-error in procedure b).

This final dependence (Fig. 3.5) gives a $m_{calc}(t)$ that matches the experimental data (Fig. 3.6). Also shown in Fig. 3.6 as dashed-line curves are $m_{calc}(t)$ for two values of constant D_{ss}, i.e. assuming that D_{ss} does not depend on solvent concentration ρ_s. These two curves with constant D_{ss} largely deviate in values and in character from the experimental curve $m_{\exp}(t)$.

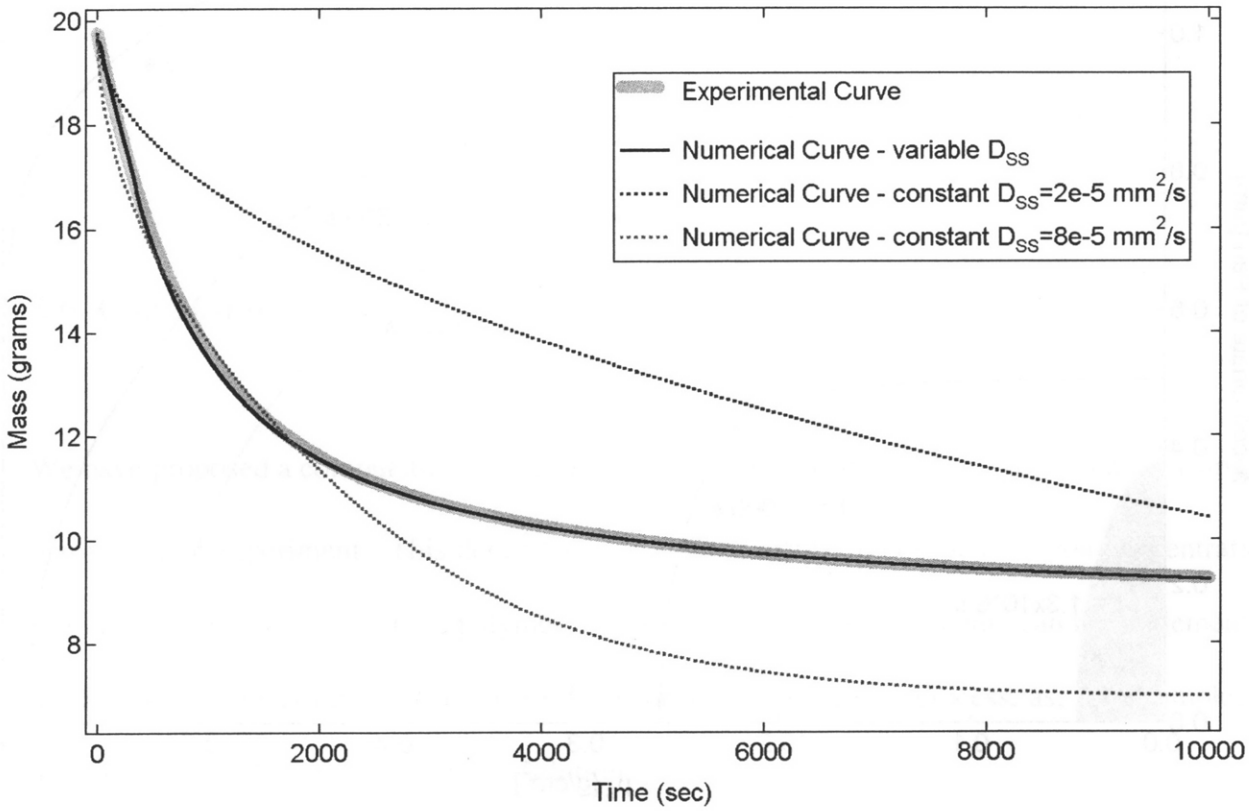

Figure 3.6. Computed mass curves obtained with constant and variable (from Fig. 3.5) diffusion coefficients, and experimental curve.

Finally, Fig. 3.7 displays several profiles of the solvent concentration ρ_s in the pan for different times. These profiles were calculated by using the $D_{ss}(\rho_s)$ relationship of Fig. 3.5. The X-coordinate corresponds to Fig. 3.2 and is essentially the pan depth coordinate, where X=0 is the bottom of the pan.

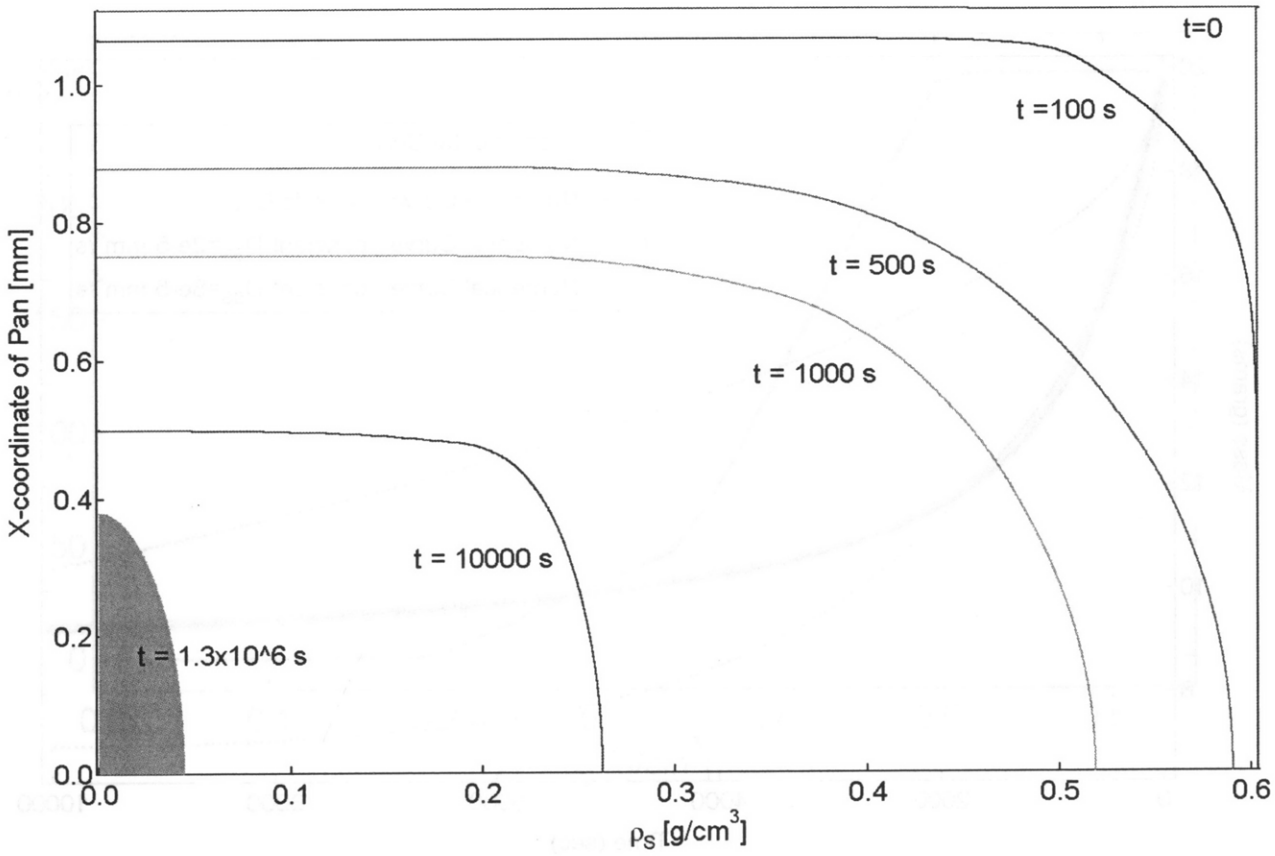

Figure 3.7 Distribution of the solvent concentration along the depth of the pan (X = 0 is the bottom of the pan, Fig. 3.2) for several times, with variable diffusion coefficient (Fig. 3.5).

As Fig. 3.7 indicates, during the process of diffusion ρ_s decreases from an initial (t=0) uniform distribution of $\rho_s = 0.603$ to smaller and smaller values as more solvent is lost. For example, after t=10000 seconds the concentration of solvent varies from 0.262 g/cm^3 at the bottom of the pan to zero at the free surface (X = 0.5mm). The shaded area under the t=1.3x10^{6}s curve represents the mass of the solvent (per unit pan cross-sectional area) left in the pan at that time. It is also worth noting that the gradient $\partial\rho_s/\partial x$ has a high value in the vicinity of the free surface in the initial period, and then decreases over time.

3.6 Conclusions

We have proposed a computational procedure for the determination of $D_{ss}(\rho_s)$ based on a simple pan-weighing experiment. This dependence of solvent diffusion coefficient upon concentration is a material characteristic of the polymer solution. The proposed procedure can be implemented in chemical engineering practice where diffusion is the governing process, as, for example, in dry spinning of fibers from a polymer solution.

It will be useful and important in future work to determine the uniqueness of the computed relation between the diffusion coefficient and the solvent concentration.

References:

[1] K. J. Bathe, The Finite Element Procedures (Prentice Hall, Englewood Cliffs, N. J., 1996).

[2] W. M. Deen, Analysis of Transport Phenomena (Oxford University Press, New York, 1998).

[3] K. H. Huebner, The Finite Element Method for Engineers (J. Wiley and Sons, New York, 1975).

[4] T. J. R Hughes, The Finite Element Method. Linear Static and Dynamic Finite Element Analysis (Prentice Hall, Englewood Cliffs, N. J., 1987).

[5] F. P. Incropera and D. P. DeWitt, Fundamentals of Heat and Mass, Fourth Edition (J. Wiley and Sons, New York, 1996).

[6] S. Kobuchi and Y. Arai, Prediction of Mutual Diffusion Coefficients for Acrylic Polymer+Organic Solvent Systems Using Free Volume Theory, Progress in Polymer Science 27 (2002) 811-814.

[7] M. Kojic, R. Slavkovic, M. Zivkovic, and N. Grujovic, PAK-T Finite Element Program for Linear and Nonlinear Heat Conduction (Univ. Kragujevac, Serbia-Yugoslavia, 1997).

[8] M. Kojic, R. Slavkovic, M. Zivkovic, and N. Grujovic, The Finite Element Method (in Serbian, Univ. Kragujevac, Serbia-Yugoslavia, 1998).

[9] M. Kojic and K. J. Bathe, Inelastic Analysis of Solids and Structures (Springer-Verlag, Goettingen, to be published).

[10] S. Middleman, An Introduction to Mass and Heat Transfer: Principles of Analysis and Design (John Wiley and Sons, New York, 1998).

[11] A. F. Mills, Heat and Mass Transfer (Richard D. Irwin, Chicago, 1995).

4 Modeling of Solvent Removal During Spinning of Synthetic Spider Silk-Like Fibers

Abstract

The process by which spiders make their mechanically superior fiber involves removal of solvent (water) from a concentrated protein solution while the solution flows through a progressively smaller diameter spinning canal. To probe the effects of solvent removal during elongational flow (which is exhibited in the spider spinning canal) on fiber mechanical properties a study using synthetic materials was conducted. The study establishes a model for solvent removal during dry spinning of synthetic fibers. The model assumes that internal diffusion governs solvent removal and that convective resistance is small. A variable internal solvent diffusion coefficient, dependent on solvent concentration, is also taken into account in the model. The synthetic polymer solution from which fibers were spun consisted of: commercially available polyurethane, resin, and solvent. An experimental setup for dry spinning into air was used to make fibers whose diameter was on the order of those made by spiders ~ 1μm. Two cases of fibers, corresponding to different spinning conditions, were numerically modeled for solvent removal and then mechanically tested. For the first case, the thicker, 40-micron fiber had relatively less solvent removal while experiencing elongational flow, than the second case 6-micron fiber. The mechanical properties of the 6-micron fiber (elastic modulus of 100 MPa and toughness of 15 MJ/m^3) were fivefold better than those of the thicker fiber indicating the

importance of solvent removal during elongational flow. Even though the mechanical properties were far from those of spider silk (modulus of 10 GPa and toughness of 150 MJ/m^3) the numerical modeling principles described in this paper could be used to help elucidate the question of how the spider makes its remarkable fiber.

4.1 Introduction

The idea of making, or spinning, a solid protein fiber out of a concentrated water solution has been utilized by spiders for millions of years [1,2]. The resulting spider-silk fiber has mechanical properties that are superior to any known material [3]. Although the chemical composition and genetic basis of the proteins have been established [4], the spinning process by which the fiber is formed remains a mystery [5,6]. During this process most of the water (solvent) is removed and simultaneously the stretched protein chains are aligned due to the elongational flow. The flow (movement of the silk solution through the spinning canal) forces the protein chains to extend along the long axis of the canal. The end result is a fiber with exceptional mechanical properties along the fiber axis [3].

By learning how the spider makes its fiber, one could conceive new processing techniques [5] that would yield novel materials, such as a synthetic spider silk analog. In order to probe how spinning factors influence fiber mechanical properties a study was performed using synthetic materials. In particular, the goal was to establish the importance of solvent removal during spinning on fiber mechanical properties.

A numerical model of solvent removal during the spinning process is proposed. The model relies on internal diffusion of solvent through the spinning solution and convective evaporation of solvent from the fiber surface. A variable internal solvent diffusion coefficient is incorporated in the model. The diffusion coefficient is dependent on solvent concentration, and this dependence is established by employing a simple pan-weighing experiment that is modeled with appropriate numerical models [13]. By using the established dependence of the diffusion coefficient on the solvent concentration, along with the boundary conditions that follow from the

relation between the internal diffusion resistance and the convective diffusion resistance (high Biot number), we have formulated a model and the corresponding numerical procedure for calculation of the solvent removal and the change in fiber radius during spinning.

A simple experimental setup consisting of a syringe pump and a rotating collection spool was constructed in order to obtain small diameter fibers that were subsequently mechanically tested. The advantages of using a synthetic material are numerous, the main being the low cost and availability. The technique used to process the synthetic polymer solution was dry spinning out of a syringe into ambient air and collection of fibers on a rotating spool. Analysis of the spinning process enabled accurate prediction of fiber mechanical properties.

The chapter is organized as follows. The next section describes the materials used and the experimental procedure. Section 4.3 contains an in depth analysis of the governing processes during solvent removal, while Section 4.4 describes the general numerical technique employed to obtained the results of Section 4.5. These results were used to predict the mechanical properties for two fibers spun under different conditions. The mechanical properties, i.e. stress-strain curves, of the fibers modeled in Section 4.5 are shown in Section 4.6. The last section has concluding remarks and touches on future work.

4.2 Materials and Experimental Procedure

A synthetic solution out of which fibers were spun consisted of three major components: polymer, resin, and solvent. The polymer used was commercial polyurethane Elasthane 80A, while the resin was PTMO-2900 (see Table 4.1). The resin's main function was to act as a plasticizer, giving a more robust spinning solution. For the solvent component, a combination of THF and DMAc was used. The recipe for the Elasthane solution is given in Table 4.1. Percentages of polymer and solvent reflect those of spider protein (spidroin) and water in the spider spinning solution (dope) [7]. The final recipe was obtained based on 'spinnability' of small diameter fibers in an effort to approach those of spider silk, which are ~ 1 micrometer.

Table 4.1 Composition of Polymer Solution

35 % Polymer *	**65 % Solvent**
20 % Elasthane 80A**	90 % THF
15 % PTMO-2900	10 % DMAc

*All percentages in weight percent.

** **Elasthane™** 80A polyurethane is a thermoplastic elastomer formed as the reaction product of a polyol, an aromatic diisocyanate, and a low molecular weight glycol used as a chain extender. Polytetramethylene oxide (PTMO) is reacted in the bulk with aromatic isocyanate, 4,4'-methylene bisphenyl diisocyanate (MDI), and chain extended with 1,4-butanediol. The Polymer Technology Group, Berkeley, California. http://www.polymertech.com/

A schematic diagram of the experimental setup is given in Fig. 4.1. The Elasthane solution (Table 4.1) was placed into a Becton-Dickinson plastic syringe (fitted with a 32 gage ¼ inch EFD dispensing needle tip) and pushed out by a KD Scientific (KDS100) syringe pump. The viscous solution was then scooped from the needle tip, stretched and placed onto the rotating collection spool. The spool consisted of a Pakon plastic slide mount (34.5mm x 23mm open area) connected to a rotating motor shaft. The spool system stands on a mobile stage, whose movement prevents fibers from folding on top of each other. In other words, the stage moves the spool in a direction perpendicular to the fiber and thus enables collection of a continuous, single fiber.

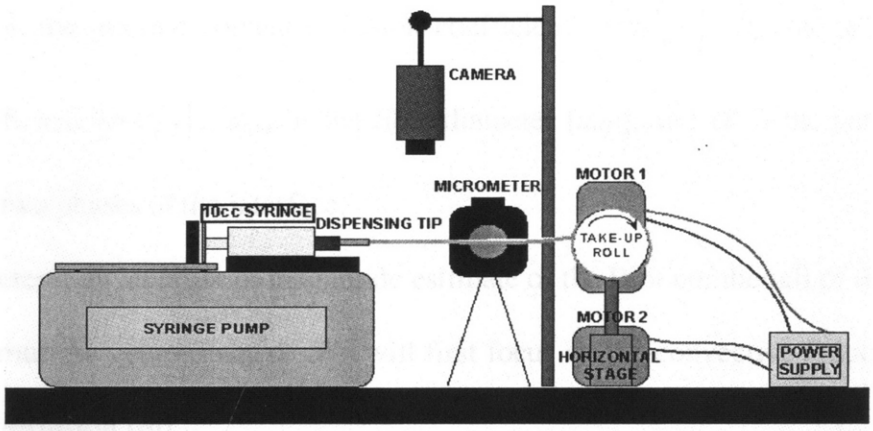

Figure 4.1 Schematic diagram of the experimental setup. The horizontal stage moves in a direction perpendicular to the page to ensure that the fiber does not wind on top of itself on the take-up roll (spool).

In any one experiment, the key adjustable parameters are: the exit velocity of the spinning solution at the needle dispensing tip (the flow rate of the solution out of the syringe divided by the cross-sectional area of the needle), the velocity of the take-up roll (spool), and the length of the spin line. We define the spin line as the path taken by the solution from its exit at the needle tip to the first point of contact with the rotating spool. The spin line represents the axial coordinate of the fiber where a velocity gradient exists, since the velocity at the spool point of contact is always greater than the needle exit velocity. Thus, the spinning solution experiences an elongational flow while on the spin line.

4.3 The Governing Process During Solvent Removal

In order for the solvent to evaporate into the surrounding air, the solvent molecules must first move through the solution and then evaporate at the air/fiber interface. The movement through the solution is controlled by internal diffusion, while the evaporation into air corresponds to external convection. To determine the relative importance of each of these two processes it is useful to look at resistances, a standard procedure in heat and mass transfer [8]. A ratio of the internal diffusion resistance to external convection resistance is defined as the mass transfer Biot number [9,10]

$$Bi_m = \frac{h_m d_{fiber} \alpha}{D_{ss}} \tag{4.1}$$

where D_{SS} is the internal solvent diffusion coefficient $\left[mm^2/s\right]$, h_m the is convective mass transfer coefficient $\left[mm/s\right]$, d_{fiber} is the fiber diameter $[mm]$, and α is the partition coefficient between the two phases at the interface.

In order to determine an order of magnitude estimate of the Biot number all of the four quantities in Eq. (4.1) must be approximated. We will first focus on the convective (vapor) side, and then examine the diffusion part.

4.3.1 The Convective Mass Transfer Coefficient

On the vapor side, for flow across a cylinder the following empirical relation holds [8]:

$$Sh_{\mathrm{Re}\to 0} = \frac{h_m d_{fiber}}{D_{sair}} \approx 0.3 \Rightarrow h_m = \frac{0.3 D_{sair}}{d_{fiber}} \tag{4.2}$$

where the dimensionless Sherwood number is the mass transfer equivalent of the Nusselt number for heat transfer, h_m is convective mass transfer coefficient $[mm/s]$, d_{fib} is the fiber diameter $[mm]$, and D_{sair} is the solvent vapor diffusion coefficient through the air $\left[mm^2/s\right]$. Also the assumption of a very small Reynold's number is justified since the air velocity (V_{air}) is small ($< 1\ m/s$) and the diameter of the fiber is on the order of microns. Hence,

$$\mathrm{Re} = \frac{V_{air} d_{fiber}}{v_{air}} \sim \frac{(1 m/s)(10^{-6} m)}{1.6\times 10^{-5} m^2/s} = 0.06 \tag{4.3}$$

where v_{air} is the kinematic viscosity for air at room temperature of T = 25°C.

To find the diffusion coefficient of solvent through the air D_{sair} in Eq. (4.2), we employ the kinetic theory of gases, which gives [11]

$$D_{sair} = \frac{0.00143\ T^{1.75}}{P M_{sair}^{0.5}\left[(\Sigma_v)_{solvent}^{1/3} + (\Sigma_v)_{air}^{1/3}\right]^2} \tag{4.4}$$

Here, D_{sair} is in $[cm/s^2]$, P is the pressure in $[bars]$, T is the temperature in $[Kelvin]$, M_{sair} is a combination of the molecular weights $[g/mol]$ of the solvent and air

$$M_{sair} = \frac{2}{(1/M_{solvent}) + (1/M_{air})} \tag{4.4b}$$

and $(\Sigma_v)_{solvent}$ and $(\Sigma_v)_{air}$ are the sum of the atomic diffusion volumes according to Fuller [11,12] for the solvent and air, respectively. For our case, after substitution of the appropriate values, Eq. (4.4) gives $D_{sair} = 10\ mm^2/s$. This value can then be substituted into Eq. (4.2) to give the convective mass transfer coefficient of $h_m = \frac{0.3\ D_{sair}}{d_{fiber}} \sim 1000\ mm/s$, since the diameter of the fiber is on the order of a micron.

4.3.2 The Internal Solvent Diffusion Coefficient

To determine the diffusion coefficient of the solvent through the solution (on the fiber side) a simple mass loss experiment was performed (Chapter 3). The goal of the experiment was to obtain the solvent diffusion coefficient as a function of solvent concentration. When concentrated polymer solutions experience significant changes in concentration due to mass transfer, the diffusion coefficient can vary considerably as a function of solvent concentration [8,10]. Using the procedure explained in Chapter 3, a small amount of the spinning solution was placed in a pan in a controlled environment, and the corresponding mass loss due to solvent evaporation was recorded. This mass loss was then modeled by numerical methods, which yielded the dependence of the solvent diffusion coefficient on solvent concentration (Fig. 4.2).

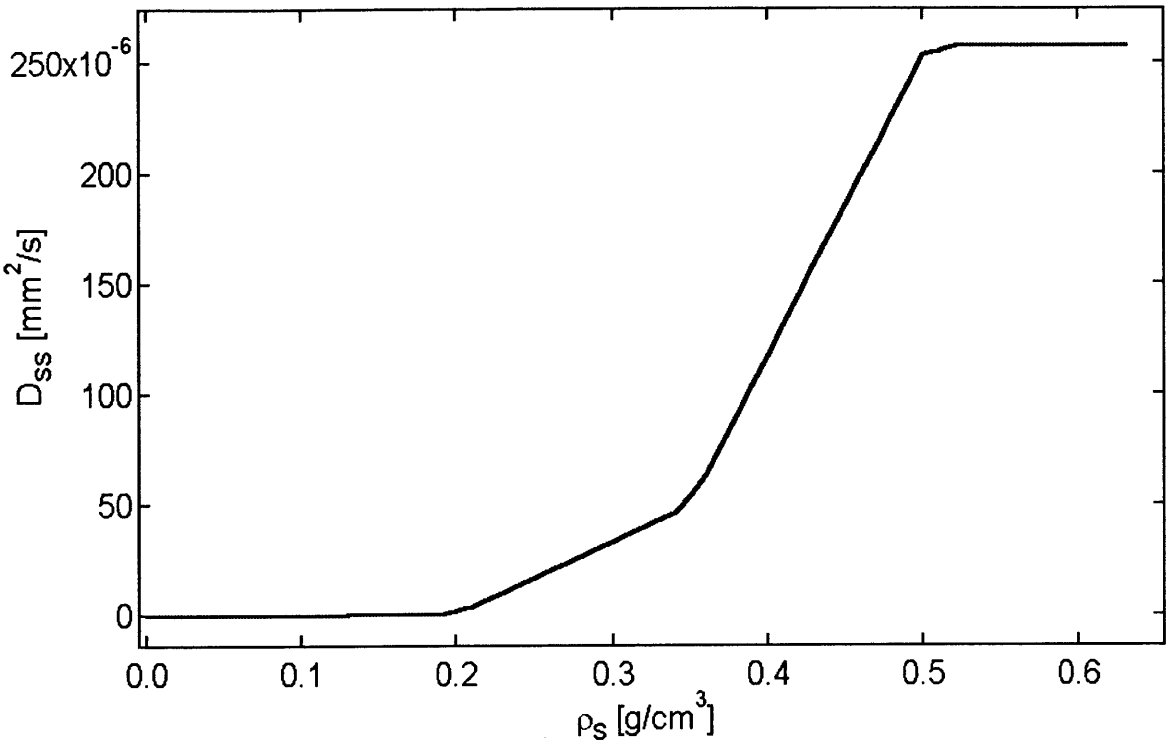

Figure 4.2 Solvent diffusion coefficient D_{ss} vs. solvent concentration ρ_s

Returning to the Biot number, all of the quantities in Eq. (4.1) can now be approximated, with the partition coefficient estimated as the ratio of the partial densities of the solvent on the liquid and vapor side ($\alpha \sim 10^{-3}$). Hence,

$$Bi_m = \frac{h_m d_{fiber} \alpha}{D_{ss}} \sim \frac{10^3 \cdot 10^{-3} \cdot 10^{-3}}{10^{-5}} = 100$$

Thus, the high value of the Biot number indicates that the internal diffusive resistance is much greater than the convective resistance. This in turn, implies that internal diffusion of solvent through the fiber solution is the governing process in solvent removal on the spin line and the convective (vapor) side can be neglected.

4.4 Numerical Modeling of Internal Solvent Diffusion

The diffusion of solvent in the case of fiber spinning can be considered as an axially symmetric process. Namely, there is axially symmetric diffusion within a fiber cross-section, with axial motion of the cross-section. The size of the cross-section decreases with time due to the solvent evaporation and due to the axial velocity gradient, as will be further described.

The diffusion of a solvent through a polymer solution is governed by Fick's law [8]

$$\frac{\partial \rho_s}{\partial t} = \nabla[\rho_T D_{ss} \nabla(\frac{\rho_s}{\rho_T})] \tag{4.5}$$

where ρ_s is the partial mass density, further referred to as concentration, of the solvent, and ρ_T is the total mass density (total mass per unit volume of solution)

$$\rho_T = \rho_s + \rho_p \tag{4.6}$$

Here ρ_p the partial mass density, or concentration of the polymer. It is assumed that the internal diffusion coefficient varies with concentration, hence at a given temperature

$$D_{ss} = D_{ss}(\rho_s) \tag{4.7}$$

In the case of axially symmetric in-plane diffusion, the system of differential equations (4.5) reduces to the differential equation [8]

$$\frac{\partial \rho_s}{\partial t} - \frac{1}{r}\frac{\partial}{\partial r}\left[r\rho_T D_{SS} \frac{\partial}{\partial r}\left(\frac{\rho_s}{\rho_T}\right)\right] = 0 \tag{4.8}$$

where r is the radial coordinate of the solution. This equation can also be written in the form of the heat conduction equation [13,14,15]

$$\frac{\partial \rho_s}{\partial t} - \frac{1}{r}\frac{\partial}{\partial r}(r\alpha_m \frac{\partial \rho_s}{\partial r}) = 0 \tag{4.9}$$

where

$$\alpha_m = \overline{\rho}_p \frac{D_{ss}}{a_1 \rho_s + \overline{\rho}_p} \tag{4.10}$$

$$a_1 = (1 - \frac{\overline{\rho}_p}{\overline{\rho}_s}) \tag{4.11}$$

and $\overline{\rho}_s$ and $\overline{\rho}_p$ are the material densities (mass per unit volume of pure substance) of the solvent and polymer, respectively. The material densities are constant and represent the material characteristics.

By using the Galerkin procedure [14,15,16] the nonlinear differential of Eq. (4.9) is transformed into the finite element balance equations, which are then linearized around the time "t" . With an implicit integration scheme, where the equilibrium is sought iteratively for the end of time step, the final incremental-iterative system of algebraic equations for the assemblage of the finite elements is obtained as [15,17,18]

$$^{t+\Delta t}\hat{\mathbf{K}}^{(i-1)} \Delta \boldsymbol{\rho}_s^{(i)} = {}^{t+\Delta t}\mathbf{F}^{(i-1)} - {}^{t+\Delta t}\hat{\mathbf{K}}^{(i-1)}\, {}^{t+\Delta t}\boldsymbol{\rho}_s^{(i-1)} \tag{4.12}$$

where "i" is the iteration counter, and the index "$t+\Delta t$" shows that the evaluation is of the matrices and vectors is performed at the end of time step. The vectors $^{t+\Delta t}\boldsymbol{\rho}_s^{(i-1)}$ and $\Delta \boldsymbol{\rho}_s^{(i)}$ are the nodal vectors for the concentrations and concentration increments. The matrix $^{t+\Delta t}\hat{\mathbf{K}}^{(i-1)}$ is

$$^{t+\Delta t}\hat{\mathbf{K}}^{(i-1)} = \frac{1}{\Delta t}\, {}^{t+\Delta t}\mathbf{M}^{(i-1)} + {}^{t+\Delta t}\mathbf{K}^{(i-1)} \tag{4.13}$$

The components of the finite element matrices are

$$^{t+\Delta t}M_{kl}^{e(i-1)} = L_x \int_{^{t+\Delta t}L^{(i-1)}} h_k h_l r dr \tag{4.14}$$

$$^{t+\Delta t}K_{kl}^{e(i-1)} = L_x \int_{^{t+\Delta t}L^{(i-1)}} \frac{\overline{\rho}_p}{\rho_T^{(i-1)}} D_{ss}^{(i-1)} \frac{\partial h_k}{\partial r} \frac{\partial h_l}{\partial r} r dr \tag{4.15}$$

where ${}^{t+\Delta t}L^{(i-1)}$ is the element length in the radial direction corresponding to the iteration "i-1" (for the first iteration , $i=1$, we use ${}^{t+\Delta t}L^{(0)}={}^{t}L$), L_x is the element length in the axial direction x, and h_k and h_l are the 1-D interpolation functions. The vector ${}^{t+\Delta t}\mathbf{F}^{(i-1)}$ is the mass flux through the element boundary at the node,

$$F_k^{(i-1)} = R_k h_k \int_{L_x} q_A dx \qquad \text{no sum on } k \tag{4.16}$$

where q_A is the mass flux through current area, R_k and h_k are the radial coordinate and the interpolation function, all corresponding to the element node. Since only in-plane diffusion is considered, then $L_x=1$. The iterations in Eq. (4.12) continue until a selected numerical tolerance is reached, e.g. $\left\|\Delta\boldsymbol{\rho}_s^{(i)}\right\| \le \varepsilon$, where ε is a small number.

The line integrals in Eq. (4.14) and (4.15) are evaluated over the last known element length ${}^{t+\Delta t}L^{(i-1)}$. This length is calculated from the element volume ${}^{t+\Delta t}V^{(i-1)}$ (with unit axial length L_x) corresponding to the solvent concentration ${}^{t+\Delta t}\rho_s^{(i-1)}$,

$${}^{t+\Delta t}V^{(i-1)} = {}^{t}V_p + \frac{2\pi}{\overline{\rho}_s} \int_{{}^{t+\Delta t}L^{(i-2)}} {}^{t+\Delta t}\rho_s^{(i-1)} r dr \tag{4.17}$$

where ${}^{t}V_p$ is volume of the polymer that corresponds to the start of time step, calculated as ${}^{t}V_p = {}^{t}V - {}^{t}V_s$, with ${}^{t}V$ and ${}^{t}V_s$ being the total volume of the finite element and the volume occupied by the solvent. It is assumed that V_p does not change within the time step Δt.

Now we consider the element lengths change, and hence the change of the fiber radius due to axial motion. In the case when the axial velocity is uniform along the fiber axis, the axial motion has no effect on the fiber radius change and the radius decrease occurs only due to solvent evaporation. However, if at a considered time and at a considered axial position of the

cross-section, the axial velocity has a non-zero axial gradient $k = \partial v/\partial x \neq 0$ ($k > 0$ for the spin line), the cross-section size changes also due to the axial motion. The fiber material can be considered incompressible, and in case of no evaporation, the mass continuity equation for two cross-sections at a distance Δx, can be written as

$$v_1 A_1 - (v_1 + k\Delta x)A_2 = 0 \tag{4.18}$$

where v_1 and A_1 are velocity and size of the first cross-section (at the position x), and A_2 is the area of the cross-section 2. The radius R_2 follows from this equation,

$$R_2 = R_1 \exp(-\frac{k\Delta x}{2v_1}) \tag{4.19}$$

and the increment Δx is

$$\Delta x = \frac{v_1}{k}(1 - \exp(-k\Delta t)) \tag{4.20}$$

The evaporation and the axial motion occur at the same time, and the diffusion depends on the current fiber radius, therefore both incompressibility and diffusion must be accounted for in a time step. We adopt the following procedure.

1. Determine the radius $R_{1/2}$ from Eq. (4.19) using $\Delta x/2$, discretize this cross-section into the finite elements, and calculate the polymer volumes ${}^{t}V_p$ for each element;
2. Calculate diffusion in the time step, starting from the radius $R_{1/2}$ and using the polymer volumes ${}^{t}V_p$. Determine the radius ${}^{t+\Delta t}R_d$ corresponding to the end of the diffusion calculations;
3. Apply the incompressibility condition (4.18) for the second half of the time step (i.e. in Eq. (4.19) substitute ${}^{t+\Delta t}R_d$ for R_1 and $\Delta x/2$ for Δx).

A graphical representation of the above steps is shown in Fig. 4.3. Note that the fiber radius at the equilibrium iteration "i" is

$$^{t+\Delta t}R^{(i)} = \sum_{elements} {}^{t+\Delta t}L^{(i)} \tag{4.21}$$

where $^{t+\Delta t}L^{(i)}$ correspond to the current element volume $^{t+\Delta t}V^{(i)}$ according to Eq. (4.17). The radius $^{t+\Delta t}R_d$ represents the final value of $^{t+\Delta t}R^{(i)}$.

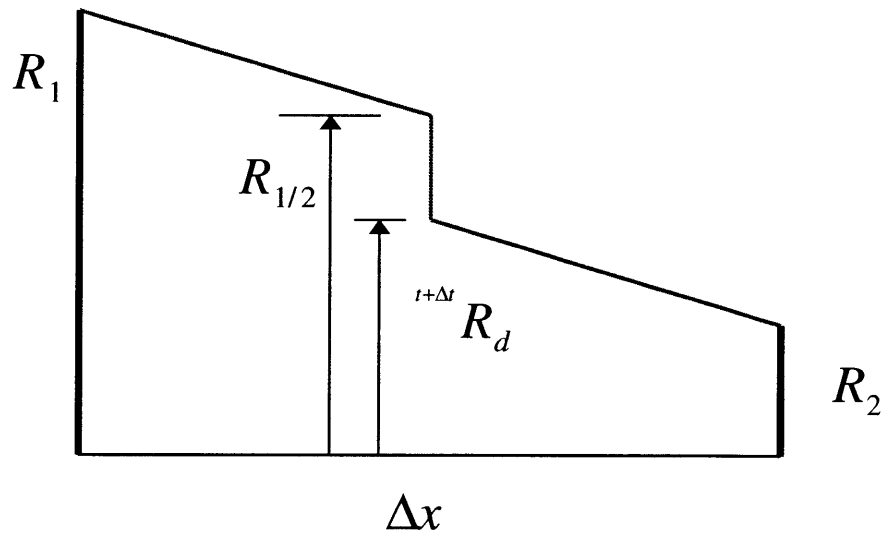

Figure 4.3 Graphical representation of the numerical procedure to take into account both diffusion and incompressibility effects during fiber spinning. The red line indicates diffusive loss (from $R_{1/2}$ to $^{t+\Delta t}R_d$), while the blue depicts incompressibility (from R_1 to $R_{1/2}$ and from $^{t+\Delta t}R_d$ to R_2)

4.5 Numerical Examples and Mechanical Properties

The general numerical procedures described in the previous section will now be applied to two cases of fiber spinning from the same material (Table 4.1), and then used to predict their corresponding mechanical properties. The material and partial densities [g/cm^3] used in Eq. (4.10) and (4.11) are

$$\bar{\rho}_s = 0.894 \qquad \bar{\rho}_p = 1$$

$$^0\rho_s = 0.603 \qquad ^0\rho_p = 0.325 \tag{4.22}$$

where the bar indicates the pure substance density, and the zero indicates the initial partial density (concentration).

The first case examined was that of relatively thick fiber and shorter spin line, while the second case models a thin fiber with a longer spin line. Specifically, the relevant data was:

Case 1) $v_{exit} = 4.7\,cm/s,\ ^0R_{fiber} = 40\mu m,\ L_{spin} = 7.5cm,\ v_{spool} = 10\,cm/s$

Case 2) $v_{exit} = 4.7\,cm/s,\ ^0R_{fiber} = 15\mu m,\ L_{spin} = 9.5cm,\ v_{spool} = 68\,cm/s$ (4.23)

Here, v_{exit} is the exit velocity out of the syringe tip, $^0R_{fiber}$ is the initial fiber diameter at a short distance from the tip (< 1mm), L_{spin} is the length of the spin line (the distance from the syringe tip to the spool), and v_{spool} is the spool speed at the point of contact of the spool and fiber (the end of the spin line).

In order to solve for the radius and concentration profiles along the spin line, an assumption that the fiber velocity increases linearly from the syringe tip to the spool was made. Thus, in (4.18)

$k = \frac{\partial v}{\partial x} = \frac{v_{spool} - v_{exit}}{L_{spin}} = const.$ Also needed was the solvent concentration boundary condition on the fiber surface $(\rho_S)_{surface} = 0$, based on the large Biot number (Section 4.3).

Following the numerical procedure described in the previous section, the modified finite element code PAK-T [19] for nonlinear heat conduction was employed for the two fiber spinning cases. The main goal was to determine how the radius and solvent concentration profiles along the spin line change under different spinning conditions. Figure 4.4 shows the results for the two cases, which differ in the length of the spin line and spool velocity. The radius change and the concentration profiles (shaded in blue) at several axial positions is shown for the two cases. Also, the ratio of ρ_{mean} / ρ_{s_0} is given for each profile as an indication of how much solvent is left, where

$$\rho_{mean} = \frac{\sum_{elements} \int_{L_{element}} \rho_s r \, dr}{R^2 \pi} \tag{4.24}$$

and ρ_{s_0} is the initial solvent concentration from Eq. (4.22), and R is the current radius (at the end of time step) of the fiber cross-section. As Fig. 4.4 indicates, at the end of the spin line the thicker fiber (case 1) has relatively almost twice as much solvent than the thinner fiber (case 2). Thus, we expect significant differences in the mechanical properties of these two fibers, since the thinner fiber was able to remove more solvent during the elongational flow experienced on the spin line. While on the spin line, the individual chains were stretched along the fiber axis and, with the simultaneous removal of solvent, able to interact with each other. The end result is an ordered structure along the fiber axis (as with a spider silk fiber) that should give good mechanical properties. It should be noted that once on the spool the fiber does not experience any change in velocity. Therefore, in the seconds subsequent to attaching to the spool the

remaining solvent evaporates and essentially "freezes" the configuration formed at the end of the spin line. In other words, since there is no more elongational flow on the spool, no further stretching of the fiber polymer chains occurs.

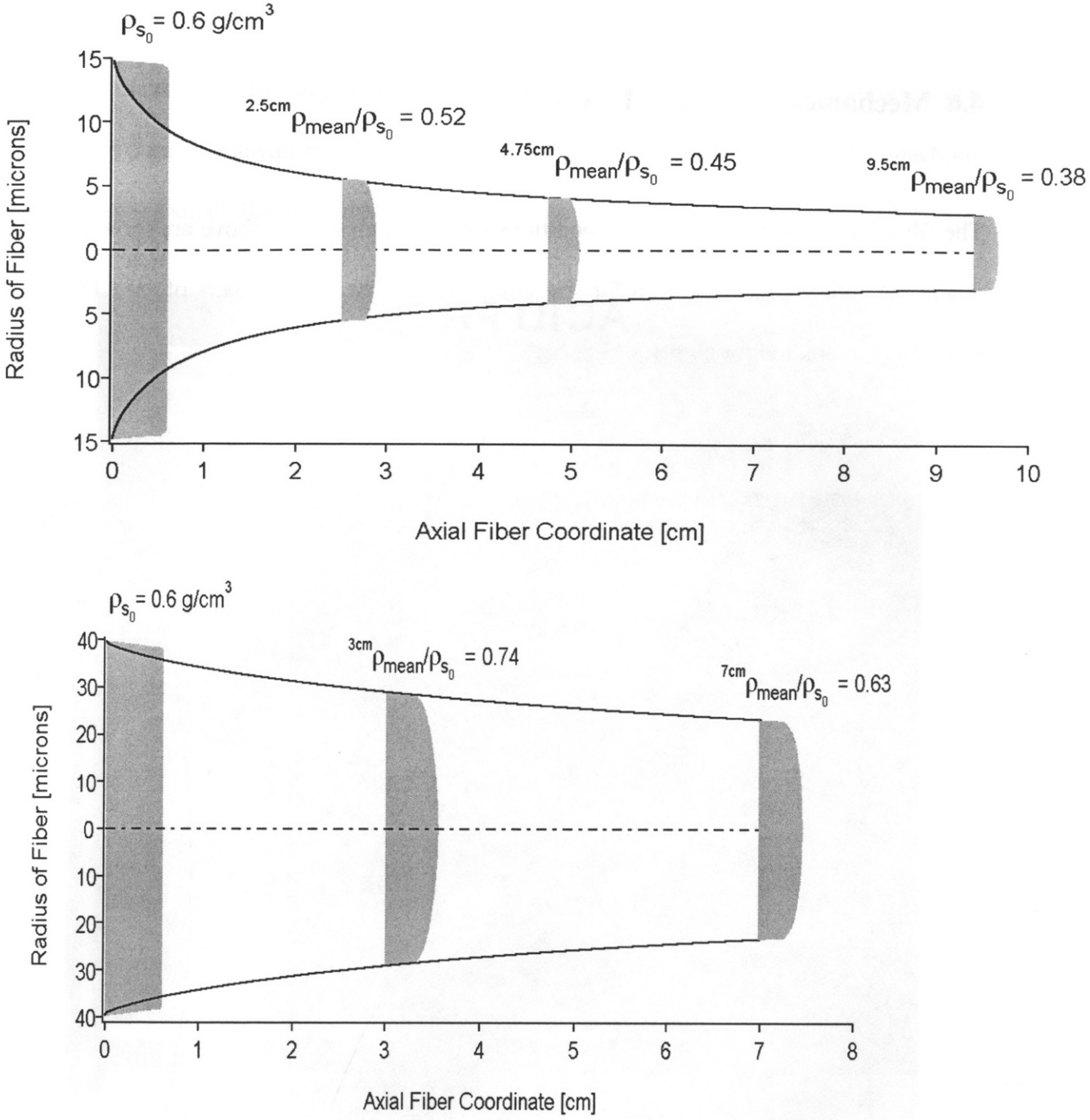

Figure 4.4 Top: Case 2) radius and concentration profiles along the spin line. Ratios of ρ_{mean} / ρ_{s_0} are given at x = 2.5 cm, x = 4.75 cm, and at the end of the spin line, x = 9.5 cm

Bottom: Case 1) radius and concentration profiles along the spin line. Ratios of ρ_{mean} / ρ_{s_0} are given at x = 3 cm and at the end of the spin line, x = 7 cm.

4.6 Mechanical Testing of Fibers

The fibers spun under the spinning conditions for case 2) described above are shown in Fig. 4.5, where the author's hair is shown for size comparison. The thicker fibers of case 1) looked the same and are omitted for clarity.

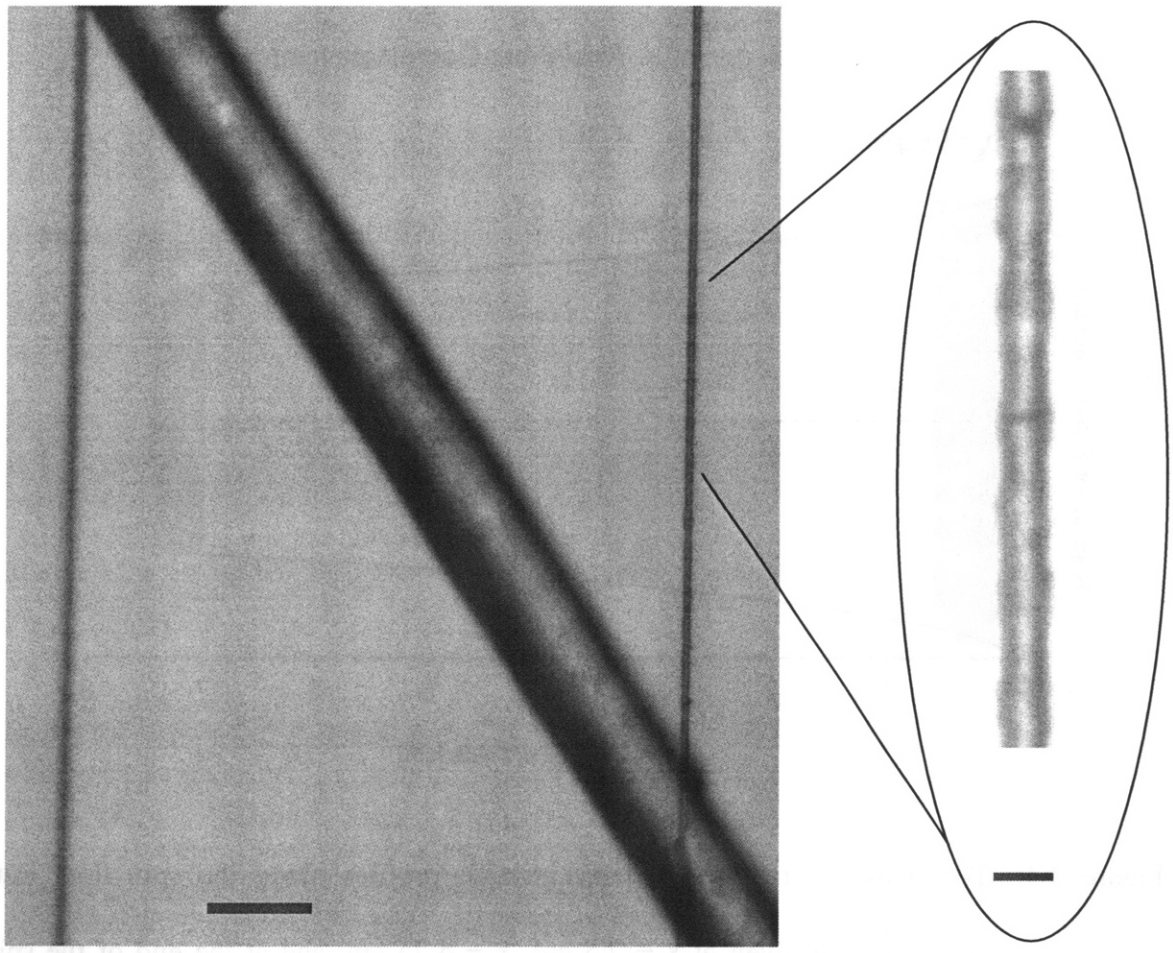

Figure 4.5 Left: a human hair between spun fibers. Bar is 80 microns.

Right: enlarged image of the spun fiber. Bar is 7 microns.

In order to determine the mechanical properties of the fibers a uniaxial testing machine developed by Sauri Gudlavalleti and Prof. Lallit Anand of MIT was used [20]. This machine is capable of testing small diameter fibers and as such was ideal for our purposes (Fig 4.6).

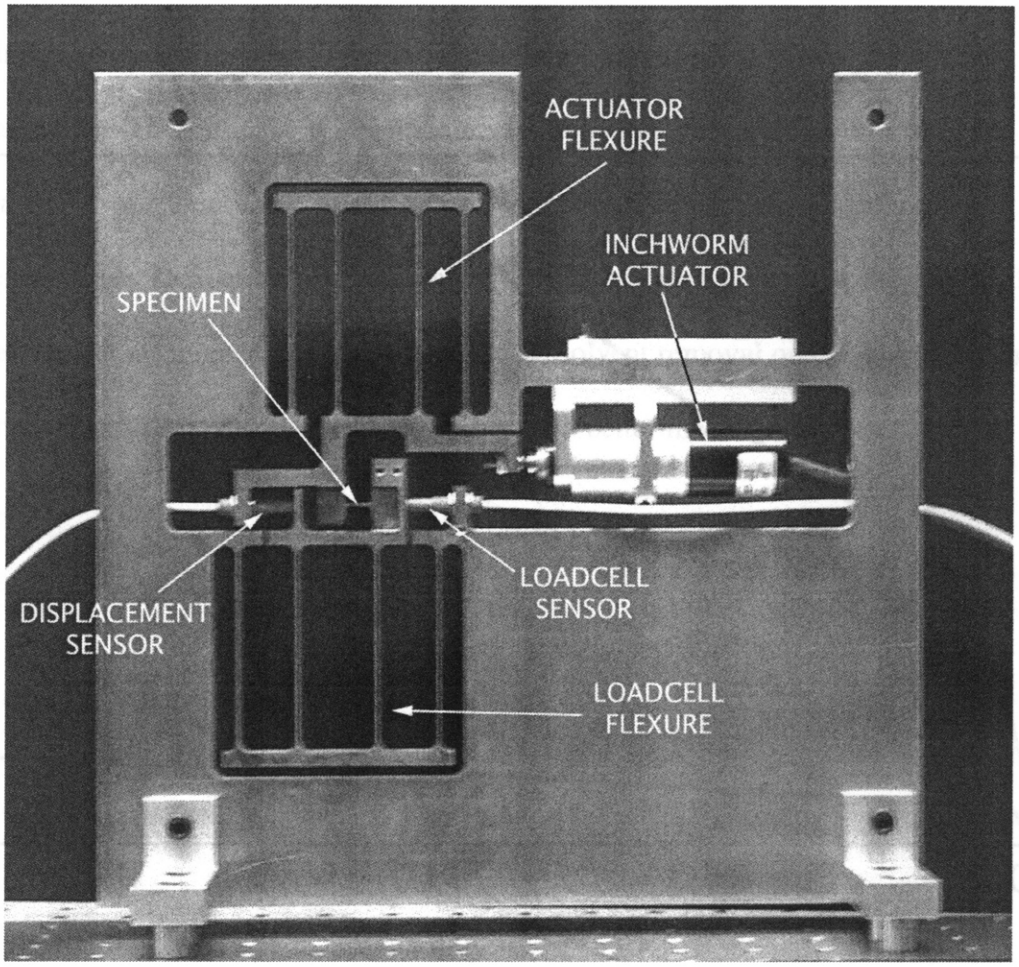

Figure 4.6 The Uniaxial Testing Machine V1. Load range: 25 μN - 1.5 N Displacement range: 20 nm – 6 mm.

The uniaxial testing machine was used to test fibers spun from case 1) and case 2). For the thin case 2) fibers, 7 fibers were placed in parallel and tested on the machine. The corresponding fiber engineering stress-strain curves for the two different cases are shown in Fig. 4.7.

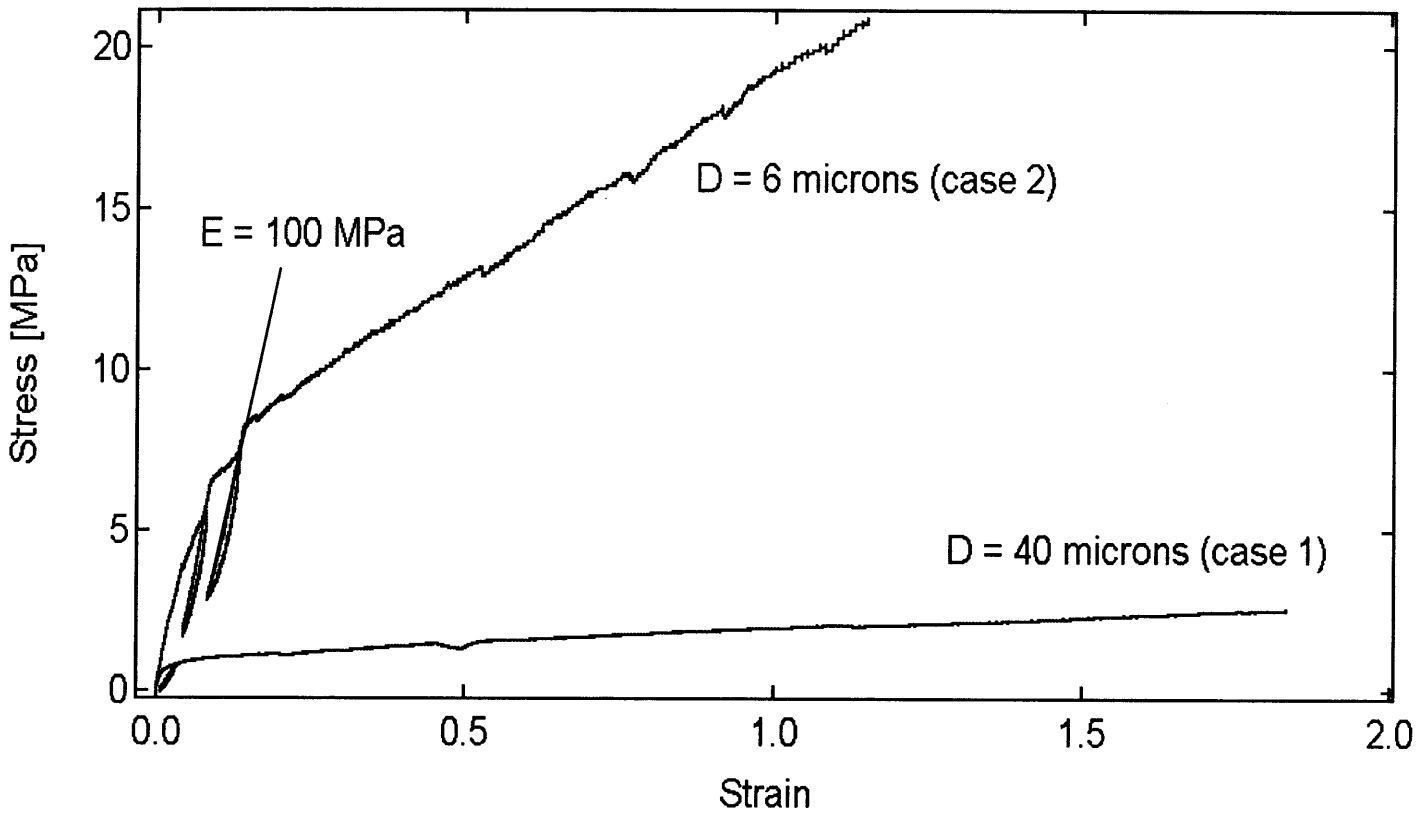

Figure 4.7 Engineering stress-strain curves for the two cases of spun fibers. The black line drawn in for case 2) corresponds to unloading the sample in the linear regime and the slope of this line is the elastic modulus E. The same graphic modulus representation for case 1) was omitted for clarity.

As expected from the analysis of the previous section, the smaller diameter fiber had considerably better mechanical properties, with an elastic modulus (E) of 100 MPa and a toughness (area under the stress-strain curve, equivalent to the energy to break) of 15 MJ/m^3. In contrast, the thicker fiber had an elastic modulus of 20 MPa and a toughness of only 3 MJ/m^3. For comparison purposes, the native spider silk dragline fiber has an elastic modulus of 10 GPa and toughness of 160 MJ/m^3 (Table 2.1) and thus is vastly superior to the synthetic fibers spun in this experiment. Nonetheless, the fiber of case 2) showed five fold better mechanical properties than the thicker case 1) fiber, which had roughly twice as much solvent at the end of the spin line. Therefore, the mechanical tests verify that more solvent removal on the spin line along with a correspondingly smaller diameter leads to a fiber with better mechanical properties.

4.7 Conclusions and Future Work

Even though the mechanical properties of the synthetic fibers were far from those of native spider silk (modulus of synthetic, case 2 fiber was only 1% and toughness was 10% to that of dragline silk) the experiments performed enabled a quantitative study of the importance of solvent removal during elongational flow on mechanical properties. A spider most likely employs a similar principle, where the spinning solution flows from the large gland reservoir through a progressively smaller diameter canal [4], in which most of the solvent is removed under an elongational flow.

The numerical procedures of this paper can be used to model solvent removal during fiber formation in the spider's canal and ultimately help elucidate the 400 million year old mechanism by which the spider makes its mechanically superior fiber.

References:

[1] Shear W.A., Palmer J.M., Coddington J.A., Bonamo P.M. A Devonian spinneret: early evidence of spiders and silk use . *Science* **246**, 479-481 (1989).

[2] Selden P.A. Orb-weaving spiders in the early Cretaceous. *Nature* **340**, 711 (1989).

[3] Gosline J.M., Guerrete P.A., Ortlepp C.S., Savage K.N. The mechanical design of spider silks: from fibroin sequence to mechanical function, *The Journal of Experimental Biology* **202**, 3295-3303 (1999).

[4] Vollrath F., Knight D.P. Liquid crystalline spinning of spider silk. *Nature* **410**, 541-548 (2001).

[5] Kaplan D., Adams W.W., Farmer B., Viney C. *Silk Polymers. Materials Science and Biotechnology* (American Chemical Society, Washington, 1994).

[6] Vollrath F., Knight D.P. Structure and function of the silk production pathway in the Spider Nephila edulis. *International Journal of Biological Macromolecules* **24**, 243-249 (1999).

[7] Chen X., Knight D.P., Vollrath F. Rheological characterization of Nephila spidroin solution. *Biomacromolecules* **3**, 644-648 (2002).

[8] Mills A.F. *Heat and mass transfer* (Richard D. Irwin, Chicago, 1995).

[9] Deen W.M. *Analysis of transport thenomena* (Oxford University Press, New York, 1998).

[10] Middleman S. *An introduction to mass and heat transfer: principles of analysis and design* (John Wiley and Sons, New York, 1998).

[11] Poling B.E., Prausnitz J.M., O'Connell J.P. *The properties of gases and liquids* (McGraw-Hill, New York, 2001).

[12] Fuller E.N., Ensley K., Giddings J.C. Diffusion of halogenated hydrocarbons in helium. The effect of structure on collision cross sections. *The Journal of Physical Chemistry* **73**, 3679-3685 (1969).

[13] Shao Z., Vollrath F. Surprising strength of silkworm silk. *Nature* **418**, p741 (2002).

[14] Huebner K.H. *The finite element method for engineers* (J. Wiley and Sons, New York, 1975).

[15] Kojic M., Slavkovic R., Zivkovic M., Grujovic M. *The finite element method* (in Serbian, University of Kragujevac, Serbia-Yugoslavia, 1998).

[16] Hughes T.J.R., *The finite element method. Linear static and dynamic finite Element Analysis* (Prentice Hall, Englewood Cliffs, N. J., 1987).

[17] Kojic M, Bathe K.J. *Inelastic analysis of solids and structures* (Springer-Verlag, Goettingen, to be published).

[18] Bathe K.J. *The finite element procedures* (Prentice Hall, Englewood Cliffs, N. J., 1996).

[19] Kojic M., Slavkovic R., Zivkovic M., Grujovic N. PAK-T Finite Element Program for Linear and Nonlinear Heat Conduction (Univ. Kragujevac, Serbia-Yugoslavia, 1997).

[20] Gudlavalleti S., Anand L. A novel testing machine for characterization of materials for MEMS applications. *Proceedings of 2001 ASME International Mechanical Engineering Congress and Exposition.*

5 *Ex Vivo* Rheology of Spider Silk

During the past decade spider silk has been revered for having unmatched mechanical properties, yet how exactly the spider makes its fiber remains unknown [1-5]. Recent studies of silkworm silk show that controlling the processing conditions of the spinning process is key to obtaining superior mechanical properties in spun silks [4]. To understand this complex flow process it is essential to elucidate the rheological properties of the initial spinning dope (a concentrated aqueous solution with 25-30 wt.% protein) stored in the spider's spinning glands [6]. Experiments performed with diluted solutions (<5 wt.%) of spider silk dope suggest non-Newtonian fluid properties [6]. However, more insight would be gained through direct rheological characterisation of the native dope. To this end, two devices were constructed: a micro-scale shear rheometer and a capillary breakup rheometer for extensional rheometry [7,8]. Both of the experimental setups were specifically designed to accommodate the small quantities (~1μL) available from the major ampullate (MA) gland of a single *Nephila clavipes* spider (Fig. 5.1), and thus enabled *ex vivo* testing of the spinning dope.

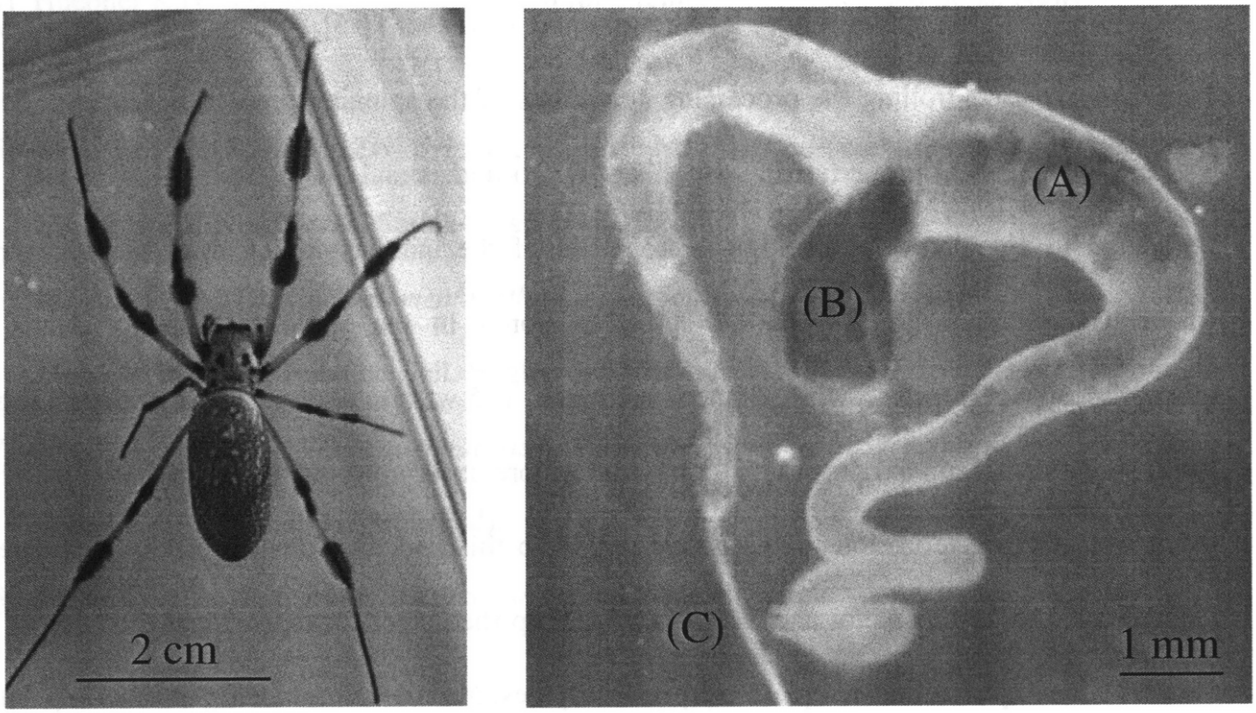

a **b**

Figure 5.1 **a,** *Nephila Clavipes* (golden-orb) spider provided by the Miami Metrozoo, Florida. Scale bar is 2cm. **b,** (A) *Major Ampullate* (MA) gland of the spider (scale bar 1 mm). The 1 μL blob (B) protruding through a rupture of the gland wall near the spinning canal (C) was used for the rheology experiments.

The micro-rheometer generates a plane Couette shearing flow between two optical flat plates separated by a precisely defined gap of 1–200 μm (Fig. 5.2a) [7]. The shear stress on the sample (from 2 to 10^4 Pa) is deduced from the deflection of the upper flexure as the lower one is actuated (shear rate in the range 2×10^{-4} - 4×10^{2} s^{-1}). This apparatus was used to measure the steady shear viscosity of a 1 μL blob of raw MA spinning dope placed between two 25 mm^2 optical plates with a gap of 25 μm. In the limit of zero shear rate, the viscosity of the spinning dope is 3500 Pa.s (Fig. 5.2b); however, the concentrated solution shear-thins significantly at higher shear rates. During a typical spinning process [4] (i.e. a flow rate of 0.25 nL/s based on a drawing speed of 20 mm/s and a thread diameter of 4μm) pushing the dope through a 40 μm-diameter canal over a distance of 20 mm would require pressures on the order of 10^8 Pa. The flow rate Q was calculated based on the thread radius and spinning velocity

$$Q = AV = \pi R^2 V = \pi\left(2\times10^{-6} m\right)^2 \left(0.02 m/s\right) \approx 0.25\times10^{-12} m^3/s = 0.25\, nL/s \qquad (5.1)$$

Using this flow rate, the pressure necessary to drive the flow was obtained from Poiseuille's Law

$$\Delta p = \frac{8Q\eta L}{\pi R^4} = \frac{8\left(0.25\times10^{-12} m^3/s\right)\left(3500 Pa\cdot s\right)\left(0.02m\right)}{\pi\left(20\times10^{-6} m\right)^4} \approx 2.8\times10^8\, Pa \qquad (5.2)$$

This pressure drop is reduced by the shear-thinning properties of the silk (the typical shear rate in the canal during spinning is 10 s^{-1}). Although shear-thinning alone does not appear to decrease the total pressure drop sufficiently, it can act synergistically with other mechanisms such as a shear-induced transition to a liquid crystalline phase [1], localised slip of the polymer solution on the tube wall, or a subtle form of lubrication, like the sericin coat surrounding fibroin fibres spun by the silkworm *Bombyx mori* [4].

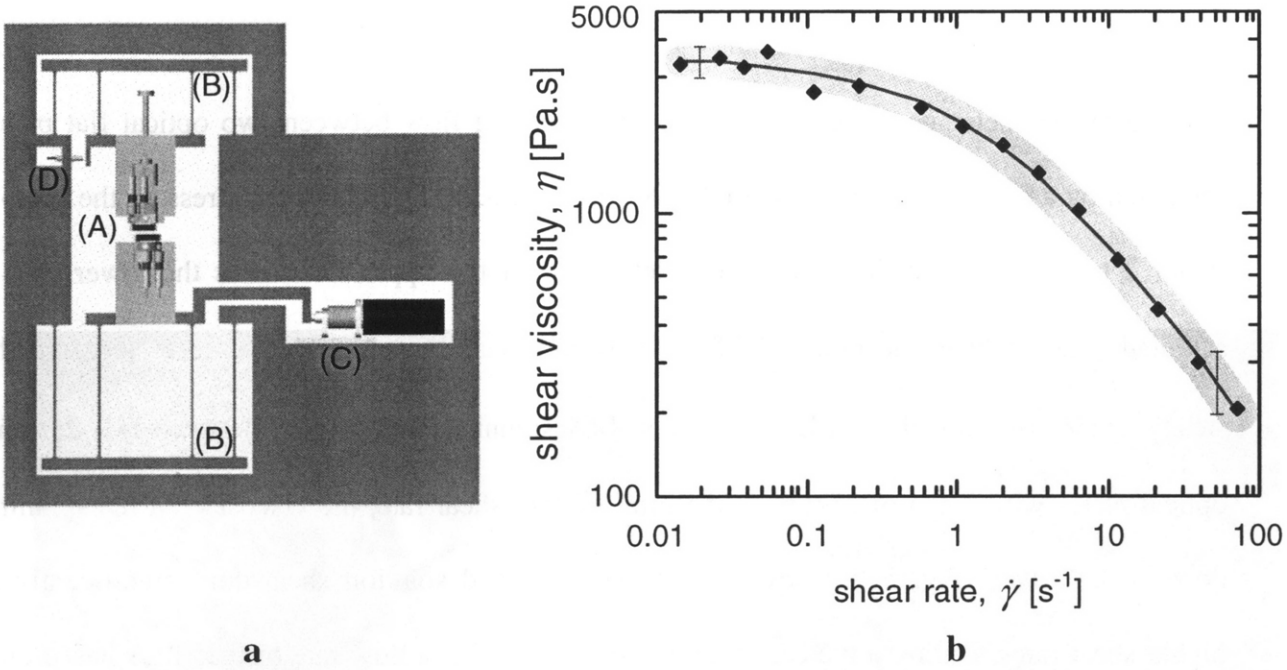

Figure 5.2 **a,** Schematic diagram of the flexure-based micro-rheometer. The fluid sample is sheared between two interferometrically aligned flat plates (A). The compound flexure system (B) is actuated by an "inchworm" motor (C) and provides a planar (Couette) shear flow. The shear stress is deduced from the corresponding deflection of the top fixture as detected by an inductive sensor (D). **b,** Shear viscosity of the raw silk dope. The shear-thinning effect is characteristic of a concentrated polymer solution and can be described by the Carreau equation, $\eta = \eta_0[1 + (\dot{\gamma}\lambda)^b]^{(n-1)/b}$, with $\eta_0 = 3500$ Pa.s, $\lambda = 0.40$ s, $b = 0.68$ and $n = 0.18$. Reproducibility was confirmed by testing specimens from two other spiders whose abdomens were similar in size. The variation in the data is represented by the shaded band and corresponds to error bars. The Weissenberg number, obtained by multiplying the relaxation time λ by the typical shear rate in the spinneret ($\dot{\gamma} \sim 10\ s^{-1}$) yields a value of $Wi = \lambda\dot{\gamma} \sim 4$, indicating viscoelastic behaviour of the dope through the spinning canal.

The dope also undergoes an elongational flow in the converging spinneret, and we have measured the transient extensional viscosity with a capillary break-up rheometer [8,9]. A 1 μL blob is placed between two 3 mm-diameter plates, which are then pulled apart to a distance of 5 mm in order to form a viscoelastic thread that necks due to capillary forces (Fig. 5.3). The extensional viscosity η_e can be deduced in this device from the pinch-off dynamics [9]: $\eta_e \approx -\sigma/(dR/dt)$ where σ is the surface tension of the liquid (estimated to be 70 mN/m, as for water) and $R(t)$ is the midpoint radius of the thread. At small strains, η_e is three times larger than the independently measured zero-shear-rate viscosity as expected for a Newtonian liquid [10]. At large strains, however, the necking dynamics are greatly retarded as the filament simultaneously strain-hardens and undergoes mass transfer (i.e. drying).

The extensional viscosity η_e for the filament was calculated from the balance of viscous and capillary forces, which including a filament geometric factor X gives [9]

$$\left.\begin{array}{l} \eta_e \dot{\varepsilon} = (2X-1)\sigma/R \\ \dot{\varepsilon} = -\dfrac{2\dot{R}}{R} \end{array}\right\} \Rightarrow \quad \dot{R} = \frac{dR}{dt} = -\frac{(2X-1)\sigma}{2\eta_e} \tag{5.3}$$

Solving then for R by integrating from the initial radius to the pinch off (R=0) gives

$$R_{initial} = \frac{(2X-1)\sigma}{2\eta_e} t_{break} = \frac{0.4254\,\sigma}{2\eta_e} t_{break} \tag{5.4}$$

where t_{break} is the time from the initial filament formation (R=$R_{initial}$) to the pinch off (R=0), and X=0.7127 was used for viscous fluid filaments [9] (for axially uniform threads X=1).

Finally, rearranging this expression yields

$$\eta_e = \frac{0.4254\,\sigma\, t_{break}}{2R_{initial}} \tag{5.5}$$

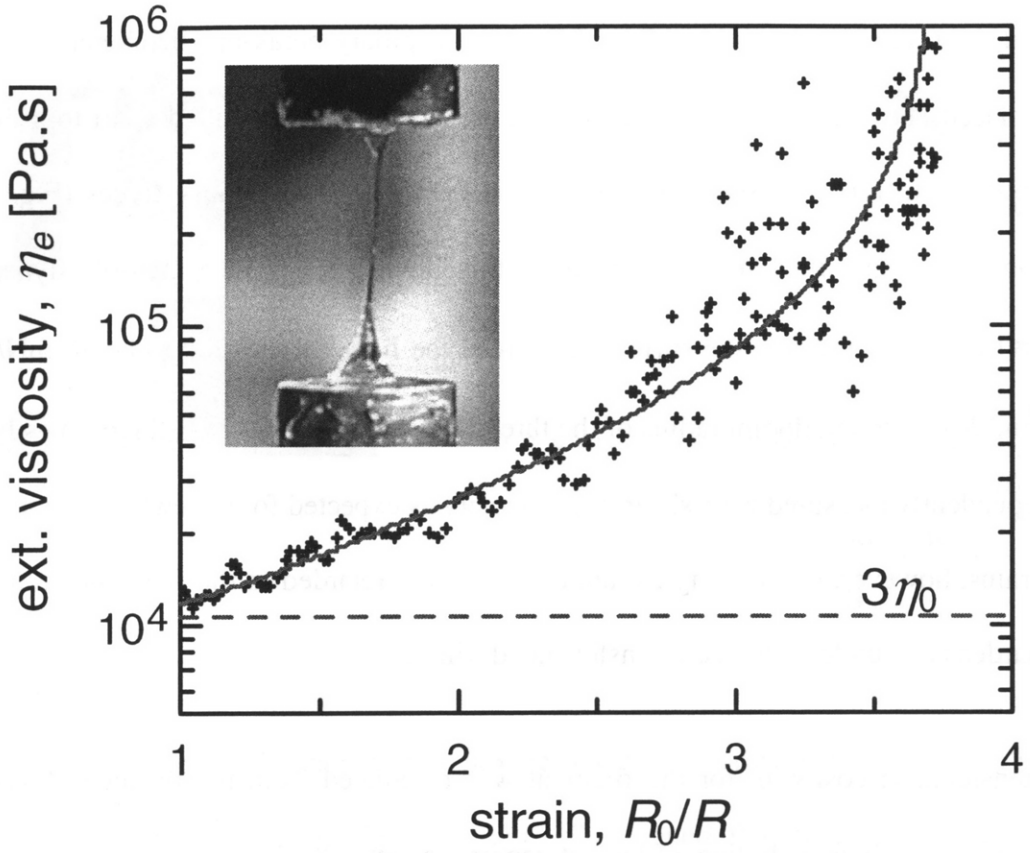

Figure 5.3 The transient extensional rheology of *ex vivo* silk dope. The extensional viscosity is shown as a function of the total strain in the material. Here, R_0 is the initial diameter of the thread measured at the midpoint between the plates with a laser micrometer. For low strains, we obtain the limit $\eta_e \approx 3\eta_0 = 11400$ Pa.s as expected for a Newtonian liquid (dashed line) [10]. Inset, a silk thread of diameter 60 μm formed by separating the plates to a distance of 5 mm and allowing the thread to neck under the action of capillarity and viscoelastic stresses.

The spinning process developed by spiders over millions of years provides a great example of a natural microfluidic system that exploits the rheology of a complex fluid. In the spinning canal, the shear viscosity decreases by an order of magnitude to reduce the required driving pressure, whereas the extensional viscosity increases by a factor of 100 to stabilise the fluid thread and inhibit breakup. Tailoring the rheological properties of artificial dopes containing genetically modified or reconstituted silks to match the *ex vivo* properties of natural silk may prove essential in enabling us to successfully process novel synthetic materials with mechanical properties comparable or better to those of spider silk.

References:

[1] Vollrath, F. & Knight, D. P. *Nature* **410,** 541–548 (2001).

[2] Kaplan, D. L., Adams, W. W., Viney, C. & Farmer, B. L. *Silk Polymers: Materials Science and Biotechnology* (ACS, Washington, 1994).

[3] Lazaris, A. *et al. Science* **295,** 472–476 (2002).

[4] Shao, Z., & Vollrath, F. *Nature* **418**, 741 (2002).

[5] Gosline, J.M., Guerrete P.A., Ortlepp C.S., Savage K.N., *J. Exp. Biol.* **202**, 3295-3303 (1999).

[6] Chen, X., Knight, D.P., Vollrath, F. *Biomacromolecules* **3**, 644-648 (2002).

[7] Gearing, B.P. & Anand, L. *Proc. of 2001 ASME Int. Mech. Eng. Congress and Exposition.*

[8] Bazilevsky, A.V., Entov, V. M. and Rozhkov, *Proc. of the Golden Jubilee meeting of the British Society of Rheology and 3rd European Rheology Conference*, Elsevier, (1990).

[9] McKinley, G.H. & Tripathi, A., *J. Rheol.*, **44**, 653-670 (2000).

[10] Trouton, F.T., *Proc. Roy. Soc. London* A , **77**, 426-440 (1906).

6 Conclusions and Future Work

The spinning of a synthetic spider silk analog would have numerous practical applications. Using an Elasthane solution small 6-micron diameter fibers were spun. These synthetic fibers were on the same scale as spider silk (~ 1 micron) and proved to be interesting for modeling effects of solvent removal during the spinning on mechanical properties. Employing numerical methods, the dependence of the solvent diffusion coefficient on solvent concentration was obtained by modeling solvent evaporation from a drop of solution placed in a small pan. The pan was in a controlled environment and from the recorded mass loss over time the diffusion coefficient was determined.

Then, knowing the diffusion coefficient dependence on solvent concentration, the solvent removal on the fiber spin line could be modeled, again using numerical methods. Two cases were examined: a thick fiber on a shorter spin line and a thin fiber on a longer spin line. The thinner fiber had relatively more solvent removed on the spin line (while experiencing elongation flow) and thus was expected to have better mechanical properties, i.e. a more aligned microstructure. Mechanical tensile tests confirmed the previous statement indicating that the thinner fiber had five fold higher toughness and elastic modulus than the thicker fiber.

The use of micro-rheometric devices enabled viscosity measurements of the spider's native spinning solution (dope). The microrheometer measured the shear thinning behavior of the *Nephila clavipes* dope, which proved to be a means of lowering the pressure required to push the liquid through the spinning canal. By using a capillary break up rheometer the extensional viscosity of the dope was obtained. For low strains the extensional viscosity was three times greater than the zero shear viscosity measured on the microrheometer, as expected for a Newtonian fluid.

In the area of synthetic fiber spinning, future work should focus on optical characterization of the spun Elasthane fibers. Optical methods, such as Fourier Transform Infrared Spectroscopy (FTIR) in conjunction with Small Angle and Wide Angle X-ray Scattering (SAXS and WAXS) could provide a way of quantifying the level of microstructural alignment along the fiber axis. Such characterization would give additional support for the idea that more solvent removal on the spin line means better alignment along the fiber axis, which in turn yields better mechanical properties.

Another interesting area for research would be the spinning of "home made" silk-like solutions, which would allow control of the polymer chemistry. By having precise control over the polymer composition one could have a variety of polymer solutions that would be application specific. In particular, a worthy challenge would be to reproduce the native spider web, requiring both synthetic dragline and viscid silk. Going one step further would be to have synthetic analogs for all seven types of spider silk and thus being able to completely mimic the spider's capabilities.

The *ex vivo* rheology can be used for exploring and understanding the spider's natural spinning process. Based on simple non-lubricated pipe flow, the spider needs to produce extremely high pressures in order to push the spinning solution through its small-diameter spinning canal. Thus, what mechanisms are employed by the spider to reduce the pressure to atmospheric (or close to atmospheric), while still being able to spin a continuous fiber, should be further examined. One way to explore these mechanisms could be to observe the pressures necessary to push the native dope through a designed canal, whose surface is lubricated. By reproducing the spinning canal surface much insight could be gained on how the spider pushes the spinning dope while removing water and achieving protein alignment along the fiber axis.